International Journal of Solids and Structures 212 (2021) 124–142

Contents lists available at ScienceDirect

International Journal of Solids and Structures

journal homepage: www.elsevier.com/locate/ijsolstr

Modeling and simulation of the non-equilibrium process for a continuous solid solution system in lithium-ion batteries

Hongjiang Chen, Hsiao-Ying Shadow Huang *

Mechanical and Aerospace Engineering Department, North Carolina State University, R3158 Engineering Building 3, Campus Box 7910, 911 Oval Drive, Raleigh, NC 27695, United States

ARTICLE INFO

Article history:
Received 14 July 2020
Received in revised form 9 November 2020
Accepted 13 November 2020
Available online 10 December 2020

Keywords:
Li-ion batteries
Solid solution system
Finite deformation
Continuum mechanics
Non-equilibrium thermodynamics
Modeling and simulation

ABSTRACT

The capacity loss and cycling aging of lithium-ion batteries at high (dis)charging rate (C-rate) hinders the development of emerging technologies. To improve the performance of Li-ion batteries, it is important to understand the coupling effect of the mechanical behaviors and the electrochemical response of electrodes, as the capacity loss and cycling aging are related to the mechanics of electrodes during (dis)charging. Many studies have formulated the distribution of stress, strain and lithium-ion fraction of electrodes during lithiation/delithiation. However, few of them reported a self-consistent formulation that contains mechanical-diffusional-electrochemical coupling effects, solid viscosity, and diffusion-induced creep for an electrode with large deformation under non-equilibrium process. This paper considers the electrode of a Li-ion battery as a solid solution system. Based on continuum mechanics, non-equilibrium thermodynamics and variational theory, we develop a generalized theory to describe the variations of stress distribution, electrode material deformation and lithium-ion fractions of the solid solution system over a non-equilibrium process. The finite deformation, mass transfer, phase transformation, chemical reaction and electrical potential of the system are coupled with each other in a fully self-consistent formulation. We apply the developed theory to numerically simulate a Sn anode particle using the finite difference method. Our results compare the influences of different C-rates on the non-equilibrium process of the anode particle. Higher C-rate corresponds to stronger dissipation effects including faster plastic deformation, larger viscous stress, more polarization in the electrical potential, longer relaxation time and less electrical energy. With the formulation and simulation of the non-equilibrium process, this study refines our understanding of the mechanical-diffusional-electrochemical coupling effect in Li-ion batteries with high C-rate.

1. Introduction

The performance and life of Li-ion batteries are related to mechanical effects of electrodes during (dis)charging (Vetter et al., 2005). For example, Wang et al. (2005) presented the crack-induced capacity fade of $LiFePO_4$ during cycling. Piper et al. (2013) reported that compressive stress may decrease the effective specific capacity of Si anodes. Cycling-induced crack propagation of a single crystal Si anode was observed and simulated by Shi et al. (2016). For decreasing the capacity loss and improving the lifetime of Li-ion batteries, it is important to understand the relation between the mechanical behaviors and the electrochemical responses of Li-ion batteries.

The mechanical behaviors of electrodes include the stress and deformation induced by the diffusion of Li. Based on the assumptions of infinitesimal deformation and diffusion of Li governed by Fick's law, the diffusion-induced stress of a spherical electrode particle was analytically solved by Cheng and Verbrugge (2009). Due to the simplicity of Fick's law, the diffusion-induced stress may be simulated conveniently for more complicated geometry of electrodes (Kim and Huang, 2016; Kim et al., 2018, 2019). However, Fick's law neglects the influence of the mechanical behaviors on the diffusion of Li. This influence may be reflected by the mechanical-chemical potential of Li which can be considered as part of the driving force of Li diffusion. To fully present the mechanical-diffusional coupling effect, some studies introduced the stress of electrode into their chemical potential models of Li (Christensen and Newman, 2006; Bower et al., 2011; Di Leo et al., 2014; Bucci et al., 2017). The stress-induced chemical potential of solid was initiated by Larché and Cahn (1973) (Eq. (1.1)):

* Corresponding author.
E-mail address: hshuang@ncsu.edu (H.-Y.S Huang).

https://doi.org/10.1016/j.ijsolstr.2020.11.014
0020-7683/

$$\mu_{\boldsymbol{\sigma}} = -\frac{1}{3} V_{PM} Tr(\boldsymbol{\sigma}) \tag{1.1}$$

where $\mu_{\boldsymbol{\sigma}}$ is stress-induced chemical potential, V_{PM} is partial molar volume, Tr is trace operator, and $\boldsymbol{\sigma}$ is stress tensor. The Larche-Cahn model is derived from the linear theory of elasticity and thus should be used based on the assumption of infinitesimal deformation. However, many alloy anodes of Li-ion batteries have large volume expansion and contraction during lithiation and delithiation, respectively (Huggins, 2008; Qi et al., 2014). In studies of modeling the finite deformation of electrodes, the mechanical-chemical potentials were formulated based on the Larche-Cahn model, even though the assumption of infinitesimal deformation is not possible (Bower et al., 2011a, 2015b, 2015c; Di Leo et al., 2014, 2015; Wen et al., 2018; Dal and Miehe, 2015; Bucci et al., 2016). A formulation for the mechanical-diffusional coupling effect of the electrodes with finite deformation is still unclear.

The diffusion of Li in an electrode is coupled with not only the mechanical behaviors but also the electrical potential of the electrode since the electrochemical reaction is related to the mechanical-chemical potential of Li. The electrode at a higher (dis)charging rate (C-rate) has more capacity loss (Kang and Ceder, 2009) and cycling aging (Xie et al., 2015), which may be related to the viscous effect of the electrode via the mechanical-chemical potential during faster deformation at the higher C-rate. The dissipation effect could become significant with larger deformation in electrodes because of their faster strain rates. However, few studies formulated the mechanical-diffusional-electrochemi cal coupling effect with solid viscosity. To this end, we adapt a non-equilibrium process with finite deformation to fully describe electrodes exhibiting different evolutions of strain and stress during lithiation/delithiation at different C-rates.

In addition, the diffusion of Li atoms can form creep strain or convection in an electrode continuum. On the scale of continuum, different atoms are indistinguishable. The stress of an electrode should be the statistical average of the atom interaction in the electrode (Thompson et al., 2009). Hence Li atoms should share the stress and be treated as a part of the electrode. The electrode mass flow induced by Li diffusion corresponds to a partial deformation of the electrode continuum. This deformation can be considered as diffusion-induced creep strain (Jones, 1965). In the measurement from Pharr et al. (2014), the variation of electrical potential of a Si film electrode demonstrated transient trend reversal with each change of C-rate. This phenomenon may be related to the diffusion induced creep strain, as C-rate can directly influence the diffusion-induced creep strain. Selecting the matrix of the electrode, such as Si atoms of Si alloy anode, as the material configuration of deformation may mathematically obviate the diffusion-induced creep strain, meanwhile the convection induced by the mass flow must be included in the formulation of electrodes. To close this knowledge gap, we consider the diffusion-induced creep strain and/or the convection effect of electrodes in the current study.

Furthermore, the diffusion of Li can generate phase separation for some electrode materials, such as $LiFePO_4$, graphite and Si (Huggins, 2008; Whittingham, 2004). The diffusion-induced stress may be influenced by the phase separation (Song et al., 2015). Many studies that considered the phase separation and the mechanical-diffusional coupling effect incorporate a sharp interface between Li-rich phase and Li-poor phase (Bower et al., 2015; ChiuHuang and Shadow Huang, 2013; Cui et al., 2013), but the sharp interface can only be applied to special geometries such as film or spherical electrodes. To address this current limitation, our study includes continuous phase field in the formulation of electrodes to present the phase separation for general geometries.

In this paper, the electrodes of Li-ion batteries are considered as solid solution systems. Based on the continuum mechanics (Sedov, 1997, 1965), non-equilibrium thermodynamics (de Groot and Mazur, 2011) and variational theory (Gelfand and Fomin, 2000), a formulation including convection effect is developed for the non-equilibrium process of a solid solution system with finite deformation. Mechanics, diffusion, phase separation, chemical reaction and electrical potential are fully coupled with each other in the formulation. We start with basic axioms such as mass conservation and the 1st law of thermodynamics to develop a general theory (Section 2.1). The general theory is then applied to a simplified Li-Sn system (Section 2.2). A system of equations is numerically solved for a Sn anode particle with an initial spherical cap geometry (Section 2.3). Our goal is to use a rigorous mathematical formulation to develop a generalized method to describe evolutions of electrochemical-mechanical behaviors of electrodes during (dis) charging at various C-rates.

2. Method

2.1. General theory

The electrodes of Li-ion batteries can be considered as continuous solid solution systems, in which every component has finite deformation due to the volume change and mass transfer during (dis)charging. In this paper, the finite deformation of an electrode system is formulated based on metric tensor (Sedov, 1997) instead of deformation gradient tensor. The deformed configurations of the solution components in the electrode are considered as deformed metric spaces with curvilinear coordinate frames, where the components of tensors generally could be covariant or contravariant. The concepts of metric tensor and covariant/contravariant components of tensors are briefly introduced in Appendix A1. Some terminologies and tensor indices are defined below: Reference space is used to refer a metric space selected for describing the components and basis of tensors. The operators and the tensor components are for the reference space unless otherwise specified. Lab space is used to refer an inertial Euclidean space with a static metric. Moreover, lowercase English letters, uppercase English or Greek letters are used with superscripts/subscripts in this paper, and details are as follows:

a. Lowercase English letters. If there is no bracket, these items are the tensors' spatial indices, and they obey Einstein's summation convention. Superscripts indicate contravariant components, and subscripts indicate covariant components.
b. Uppercase English or Greek letters. Normal superscripts/-subscripts of a variable. They are not indices and do not obey Einstein's summation convention.
c. Within brackets. Indices that do not obey Einstein's summation convention.

2.1.1. Mass conservation and kinematics of continuums for solution systems

A solution system is composed of different matter components k. Every component corresponds to an individual continuous metric space, which can move and deform following the movement of a corresponding component relative to a static space. In general, due to the movement of the components, the coordinate frames of the corresponding spaces are curvilinear. We may select the metric space corresponding to any component as the reference space, in which the Lagrangian coordinate is used for the selected component and the Eulerian coordinate is used for all other components. In this paper, the term "velocity" is the velocity relative to the selected reference space unless otherwise specified. In addition, the lab space is necessary for describing the deformation of a solution system.

Based on mass conservation, the divergence theorem and the chain rule yield equation (2.1.1) used for the density change in component k. The derivation steps are shown in Appendix A2. As shown in equation (2.1.1), the local change rate in the density for component k is caused by the convective change rate of the density $\nabla\cdot\left(\rho_{(k)}\boldsymbol{v}_{(k)}\right)$, the deformation of the reference space $\nabla\cdot\underset{\sim}{\boldsymbol{v}}$, and local chemical reactions $\sum_j \xi_{(k)}^{(j)}J^{(j)}$.

$$\frac{\partial\rho_{(k)}}{\partial t}+\nabla\cdot\left(\rho_{(k)}\boldsymbol{v}_{(k)}\right)+\rho_{(k)}\nabla\cdot\underset{\sim}{\boldsymbol{v}}=\sum_j \xi_{(k)}^{(j)}J^{(j)} \tag{2.1.1}$$

where $\rho_{(k)}$ is the mass density of component k, $\boldsymbol{v}_{(k)}$ is the velocity of component k in the solution system, $\nabla\cdot$ is divergence operator, $\underset{\sim}{\boldsymbol{v}}$ is the velocity of the reference space relative to the lab space, $\xi_{(k)}^{(j)}$ is the mass stoichiometric ratio of component k in chemical reaction j, which is less than zero for the components on the left of the chemical equation, and $J^{(j)}$ is the chemical reaction mass rate of reaction$j$.

To describe the diffusion of components in a solution system, we introduce a mass center continuum for the solution system, in which the density and velocity are defined as follows:

$$\rho=\sum_k \rho_{(k)} \tag{2.1.2}$$

$$\rho\boldsymbol{v}=\sum_k \rho_{(k)}\boldsymbol{v}_{(k)} \tag{2.1.3}$$

where ρ and $\boldsymbol{v}$ are the density and the velocity of the mass center continuum, which are called the mass center density and the mass center velocity, respectively (Sedov, 1997).

The diffusion flux and the mass fraction of component k are defined as follows:

$$\boldsymbol{J}_{(k)}=\rho_{(k)}\left(\boldsymbol{v}_{(k)}-\boldsymbol{v}\right) \tag{2.1.4}$$

$$x_{(k)}=\rho_{(k)}/\rho \tag{2.1.5}$$

where $\boldsymbol{J}_{(k)}$ and $x_{(k)}$ are the flux and the mass fraction of component k, respectively (Sedov, 1997).

With equations (2.1.2) and (2.1.3), summing (2.1.1) for all the k components yields equation (2.1.6), which describes the density change of the mass center continuum. Because all the components satisfy the conditions for mass conservation, the mass center continuum is also mass-conserved. The chemical reactions are mass-conserved, and hence are canceled by the summation, as shown in equation (2.1.6):

$$\frac{\partial\rho}{\partial t}+\nabla\cdot(\rho\boldsymbol{v})+\rho\,\nabla\cdot\underset{\sim}{\boldsymbol{v}}=0 \tag{2.1.6}$$

Combining equations (2.1.6) and (2.1.1) yields equation (2.1.7) with equation (2.1.8) below for the changing rate of the mass fraction:

$$\rho\dot{x}_{(k)}+\nabla\cdot\boldsymbol{J}_{(k)}=\sum_j \xi_{(k)}^{(j)}J^{(j)} \tag{2.1.7}$$

$$\dot{x}_{(k)}=\frac{dx_{(k)}}{dt} \tag{2.1.8}$$

where $\cdot$ is the operator of rate, and $\frac{d}{dt}$ is the total derivative operator over time of a tensor's components for fixed mass center coordinates. In the selected reference space, the total derivatives for functions of coordinate z^i and time t are calculated by the equation (2.1.9) below,

$$\frac{d}{dt}=\frac{\partial}{\partial t}+v^i\frac{\partial}{\partial z^i} \tag{2.1.9}$$

where v^i is the contravariant component of the mass center velocity and z^i is the contravariant coordinate of the selected reference space.

The covariant component of the strain tensor for a continuum is defined as half of the change in the covariant component of the metric for the corresponding space (Sedov, 1997). Equation (2.1.10) shows the strain of the mass center continuum:

$$\hat{\varepsilon}_{ij}=\frac{1}{2}\left(\hat{g}_{ij}-g^{\circ}{}_{ij}\right) \tag{2.1.10}$$

where $\hat{\varepsilon}_{ij}$ is the covariant component of the strain tensor for the mass center continuum. ^ indicates that the component corresponds to the mass center space, $\hat{g}_{ij}$ is the covariant component of the metric tensor of the deformed mass center space, and $g^{\circ}{}_{ij}$ is the covariant component of the metric tensor for the initial mass center space. Above metric-based definition of strain for the finite deformation can be applied to the strains in different categories (Sedov, 1997): elastic strain, thermal strain, plastic strain, concentration strain, etc. As proved in Appendix A1, the strain tensor defined by equation (2.1.10) is equivalent to the Green strain tensor.

The total strain may be composed of multiple strains with different categories, which can be elastic, plastic, creep, etc. For the mass center continuum, within the mass center space, the covariant component of the total strain is the summation of the covariant components of the strains in all categories (Sedov, 1997), as shown in equation (2.1.11):

$$\hat{\varepsilon}_{ij}=\sum_l \hat{\varepsilon}_{ij}^{(l)} \tag{2.1.11}$$

where $\hat{\varepsilon}_{ij}^{(l)}$ is the component of the strain for the mass center space with category l, and the category may be elastic, plastic, creep, etc. Based on the metric-based definition of strain demonstrated by equation (2.1.10), the additive decomposition of strain component shown by equation (2.1.11) is valid for the finite deformation and consistent with the multiplicative decomposition of deformation gradient, which is proved in Appendix A1. Please note that only the covariant components in Lagrangian coordinates satisfy the additive decomposition of strain component (Sedov, 1997).

2.1.2. Momentum equation and energy equation

The Cauchy stress in a solution system represents the statistical average of the atom interaction in the system (Thompson et al., 2009). As the atoms of all the components are indistinguishable on continuous scale, the Cauchy stress is related to the acceleration of the mass center continuum using the momentum equation as shown below (de Groot and Mazur, 2011);

$$\rho\boldsymbol{a}^L=\nabla\cdot\boldsymbol{p}+\sum_k \rho_{(k)}\boldsymbol{F}_{(k)}^L \tag{2.1.12}$$

where $\boldsymbol{a}^L$ is the acceleration of the mass center continuum relative to the lab space, $\boldsymbol{p}$ is the Cauchy's stress tensor of the solution system, and $\boldsymbol{F}_{(k)}^L$ is the specific body force of component k in the lab space.

In the reference space, $\boldsymbol{a}^L$ is calculated using equation (2.1.13):

$$a^{Li}=\frac{\partial v^{Li}}{\partial t}+v^{Lk}\nabla_k v^{Li} \tag{2.1.13}$$

where a^{Li} is the contravariant component of $\boldsymbol{a}^L$, v^{Li} is the contravariant component of $\boldsymbol{v}^L$, which is the velocity of the mass center continuum relative to the lab space, and ∇_k is the operator of the covariant derivative.

The evolution of the solution system obeys the 1st law of thermodynamics. The energy equation of the system is formulated using the generalized D'Alembert principle below:

$$\delta\int_V u\rho dV=\int_V \delta q\rho dV+\int_V\sum_k \rho_{(k)}\boldsymbol{F}^L_{(k)}\cdot\delta\boldsymbol{r}^L_{(k)}dV+\delta W_a+\int_A \boldsymbol{p}\cdot\boldsymbol{n}\cdot\delta\boldsymbol{r}^L dA \tag{2.1.14}$$

where u is the specific internal energy of the mass center continuum, V is the volume of the solution system, q is the specific heat of the mass center continuum, $\delta\boldsymbol{r}^L_{(k)}$ is the variational of the radius vector for component k in the lab space, δW_a is the total virtual work of inertia force in the system, $\boldsymbol{n}$ is the normal vector for the surface of the solution system, $\delta\boldsymbol{r}^L$ is the variational of the radius vector for the mass center continuum in the lab space, and A is the surface area of the solution system.

On the continuous scale, we use the mass center continuum to represent the entire solution system. The mass center density and the mass center velocity are considered as the density and the velocity of the system, respectively. Hence, we use the mass center continuum to calculate the virtual work of the inertia force in equation (2.1.14), as shown below:

$$\delta W_a=\int_V -\rho\boldsymbol{a}^L\cdot\delta\boldsymbol{r}^L dV \tag{2.1.15}$$

2.1.3. Equation of the entropy production rate

The evolution of a solution system satisfies the 2nd law of thermodynamics. Under nonequilibrium thermodynamics, the entropy production rate is composed of a series of generalized thermodynamic flows and forces that describe the system at nonequilibrium (de Groot and Mazur, 2011). The derivation of the entropy production rate is based on the description of the internal energy. The solution system is represented by its mass center continuum, of which the total internal energy is a functional of the specific internal energy, which is shown in equation (2.1.16):

$$U=\int_m u\left(s,\ \hat{\varepsilon}^{(l)}_{ij},\ \hat{\nabla}_k\hat{\varepsilon}^{(l)}_{ij},\ x_{(k)},\ \hat{\nabla}_i x_{(k)}\right)dm \tag{2.1.16}$$

where U is the total internal energy of the solution system, s is specific entropy, $\hat{\nabla}_i$ is the operator of the covariant derivative in the mass center space, and m is the mass of the solution system.

The intensive thermodynamic functions of the solution system are defined as the functional derivatives of the total internal energy. With the mathematical relation between the functional derivatives and the partial derivatives, we define the homogeneous functions and inhomogeneous functions as shown below:

Temperature T is defined as follows:

$$T=\left(\frac{\delta U}{\delta s}\right)_{\boldsymbol{\varepsilon},x}=\left(\frac{\partial u}{\partial s}\right)_{\boldsymbol{\varepsilon},\nabla\boldsymbol{\varepsilon},x,\nabla x} \tag{2.1.17}$$

Stress with category l, $\boldsymbol{\sigma}^{(l)}$, is defined as follows:

$$\frac{1}{\rho}\hat{\sigma}^{(l)ij}=\left(\frac{\delta U}{\delta\hat{\varepsilon}^{(l)}_{ij}}\right)_{s,\boldsymbol{\varepsilon}^{(l'\neq l)},x}=\frac{1}{\rho}\hat{\sigma}^{(l)ij}_{HOM}-\hat{\nabla}_k\frac{1}{\rho}\hat{\sigma}^{(l)ijk}_{INH} \tag{2.1.18}$$

With category l, the homogeneous stress $\boldsymbol{\sigma}^{(l)}_{HOM}$ and the inhomogeneous stress $\boldsymbol{\sigma}^{(l)}_{INH}$ are defined below, respectively:

$$\frac{1}{\rho}\hat{\sigma}^{(l)ij}_{HOM}=\left(\frac{\partial u}{\partial\hat{\varepsilon}^{(l)}_{ij}}\right)_{s,\boldsymbol{\varepsilon}^{(l'\neq l)},\nabla\boldsymbol{\varepsilon},x,\nabla x} \tag{2.1.19}$$

$$\frac{1}{\rho}\hat{\sigma}^{(l)ijk}_{INH}=\left(\frac{\partial u}{\partial\hat{\nabla}_k\hat{\varepsilon}^{(l)}_{ij}}\right)_{s,\varepsilon,\nabla\varepsilon^{(l'\neq l)},x,\nabla x} \tag{2.1.20}$$

The category l can be elastic, plastic, creep, etc. The chemical potential of component k relative to component K is defined by

$$\mu_{(kK)}=\left(\frac{\delta U}{\delta x_{(k)}}\right)_{s,\boldsymbol{\varepsilon},x_{(k'\neq k)}}=\mu_{HOM(kK)}-\hat{\nabla}_i\hat{\mu}^i_{INH(kK)} \tag{2.1.21}$$

where the homogeneous relative chemical potential $\mu_{HOM(kK)}$ and inhomogeneous relative chemical potential $\boldsymbol{\mu}_{INH(kK)}$ are respectively defined by:

$$\mu_{HOM(kK)}=\left(\frac{\partial u}{\partial x_{(k)}}\right)_{s,\boldsymbol{\varepsilon},\nabla\boldsymbol{\varepsilon},x_{(k'\neq k)},\nabla x} \tag{2.1.22}$$

$$\hat{\mu}^i_{INH(kK)}=\left(\frac{\partial u}{\partial\hat{\nabla}_i x_{(k)}}\right)_{s,\boldsymbol{\varepsilon},\nabla\boldsymbol{\varepsilon},x,\nabla x_{(k'\neq k)}} \tag{2.1.23}$$

Based on the definitions of the intensive functions above, we find equations (2.1.24), (2.1.25), (2.1.26), (2.1.27), and (2.1.28) for the entropy production rate by combining the conservation equation (2.1.7), the energy equation (2.1.14), and the divergence theorem. The derivation steps are shown in Appendix A3. With equation (2.1.24), we have the generalized thermodynamic flows $\boldsymbol{J}_s$, $\boldsymbol{\tau}^{(l)}$, $\boldsymbol{J}_{(k)}$, and $J^{(j)}$, and generalized thermodynamic forces ∇T, $\dot{\boldsymbol{e}}^{(l)}$, $\nabla\Psi^L_{(kK)}$, and $A^{(j)}_C$ (de Groot and Mazur, 2011). The generalized thermodynamic flows can be expressed as functions of the generalized thermodynamic forces. Their models for a simplified case are shown in Section 2.2.2.

$$T\theta=-J_s\cdot\nabla T+\sum_l\tau^{(l)}:\dot{e}^{(l)}-\sum_k^{K-1}J_{(k)}\cdot\nabla\Psi^L_{(kK)}+\sum_j J^{(j)}A^{(j)}_C \tag{2.1.24}$$

$$\tau^{(l)}=p-\sigma^{(l)} \tag{2.1.25}$$

$$\Psi^L_{(kK)}=\mu_{(kK)}+\varphi^L_{(kK)} \tag{2.1.26}$$

$$F^L_{(kK)}=F^L_{(k)}-F^L_{(K)}=-\nabla\varphi^L_{(kK)} \tag{2.1.27}$$

$$A^{(j)}_C=-\sum_k^{K-1}\mu_{(kK)}\xi^{(j)}_{(k)} \tag{2.1.28}$$

where θ is entropy production rate, $\boldsymbol{J}_s$ is entropy flux, $\boldsymbol{\tau}^{(l)}$ is the dissipation stress with category l, $\dot{\boldsymbol{e}}^{(l)}$ is the strain rate with category l of the mass center continuum, $\boldsymbol{J}_{(k)}$ is the diffusion flux of component k, $\Psi^L_{(kK)}$ is the potential energy of component k relative to component K in the lab space, $A^{(j)}_C$ is the specific chemical affinity of reaction j, and $\varphi^L_{(kK)}$ is the potential energy corresponding to the body force in the lab space.

2.1.4. Constitutive relations of state functions

We selected T, $\boldsymbol{\varepsilon}^{(l)}$, $\nabla\boldsymbol{\varepsilon}^{(l)}$, $x_{(k)}$, and $\nabla x_{(k)}$ as the basic independent parameters to determine the status of a solution system. The other state functions of the solution system depend on these five parameters. To replace the specific entropy with the temperature as an independent parameter of the state functions in Section 2.1.3, specific free energy a_F is introduced by equations (2.1.29) and (2.1.30):

$$a_F=u-Ts \tag{2.1.29}$$

and

$$da_F=-sdT+\sum_l\frac{1}{\rho}\hat{\sigma}^{(l)ij}_{HOM}d\hat{\varepsilon}^{(l)}_{ij}+\sum_l\frac{1}{\rho}\hat{\sigma}^{(l)ijk}_{INH}d\hat{\nabla}_k\hat{\varepsilon}^{(l)}_{ij}+\sum_k^{K-1}\mu_{HOM(kK)}dx_{(k)}+\sum_k^{K-1}\hat{\mu}^i_{INH(kK)}d\hat{\nabla}_i x_{(k)} \tag{2.1.30}$$

We assume that the 2nd order partial derivatives of a_F is continuous. The homogeneous and inhomogeneous stresses are therefore a continuous function of T, $\boldsymbol{\varepsilon}^{(l)}, \nabla\boldsymbol{\varepsilon}^{(l)}, x_{(k)}$, and $\nabla x_{(k)}$. It is assumed that there is no crossed coupling between different categories of the (in)homogeneous stresses, i.e., $\left(\frac{\partial\left(\hat{\sigma}^{(l)ij}_{HOM}/\rho\right)}{\partial\hat{\varepsilon}^{(h)}_{kl}}\right)_{l\neq h}=0$, $\left(\frac{\partial\left(\hat{\sigma}^{(l)ij}_{HOM}/\rho\right)}{\partial\hat{\nabla}_m\hat{\varepsilon}^{(h)}_{pq}}\right)_{l\neq h}=0$, $\left(\frac{\partial\left(\hat{\sigma}^{(l)ijk}_{INH}/\rho\right)}{\partial\hat{\varepsilon}^{(h)}_{pq}}\right)_{l\neq h}=0$, and $\left(\frac{\partial\left(\hat{\sigma}^{(l)ijk}_{INH}/\rho\right)}{\partial\hat{\nabla}_m\hat{\varepsilon}^{(h)}_{pq}}\right)_{l\neq h}=0$. The homogeneous and inhomogeneous stresses with category l satisfy equations (2.1.31) and (2.1.32):

$$d\left(\frac{\hat{\sigma}^{(l)ij}_{HOM}}{\rho}\right)=\hat{C}^{(l)ijkl}_{\rho}d\hat{\varepsilon}^{(l)}_{kl}+\hat{C}^{(l)ijrsp}_{\rho\nabla}d\hat{\nabla}_p\hat{\varepsilon}^{(l)}_{rs}+\sum_{k}^{K-1}\hat{\kappa}^{(l)ij}_{(kK)}dx_{(k)}+\sum_{k}^{K-1}\hat{\kappa}^{(l)ijq}_{\nabla(kK)}d\hat{\nabla}_q x_{(k)}+\hat{\gamma}^{(l)ij}dT \tag{2.1.31}$$

and

$$d\left(\frac{\hat{\sigma}^{(l)ijk}_{INH}}{\rho}\right)=\hat{\Lambda}^{(l)ijklm}d\hat{\varepsilon}^{(l)}_{lm}+\hat{\Lambda}^{(l)ijklmp}_{\nabla}d\hat{\nabla}_p\hat{\varepsilon}^{(l)}_{lm}+\sum_{k}^{K-1}\hat{\omega}^{(l)ijk}_{(kK)}dx_{(k)}+\sum_{k}^{K-1}\hat{\omega}^{(l)ijkq}_{\nabla(kK)}d\hat{\nabla}_q x_{(k)}+\hat{\chi}^{(l)ijk}dT \tag{2.1.32}$$

where $\hat{C}^{(l)ijkl}_{\rho}$, $\hat{C}^{(l)ijrsp}_{\rho\nabla}$, $\hat{\kappa}^{(l)ij}_{(kK)}$, $\hat{\kappa}^{(l)ijq}_{\nabla(kK)}$, $\hat{\gamma}^{(l)ij}$, $\hat{\Lambda}^{(l)ijklm}$, $\hat{\Lambda}^{(l)ijklmp}_{\nabla}$, $\hat{\omega}^{(l)ijk}_{(kK)}$, $\hat{\omega}^{(l)ijkq}_{\nabla(kK)}$, and $\hat{\chi}^{(l)ijk}$ are the components of the coefficient tensors.

Similarly, the relative chemical potentials are continuous functions of T, $\boldsymbol{\varepsilon}^{(l)}$, $\nabla\boldsymbol{\varepsilon}^{(l)}$, $x_{(k)}$, and $\nabla x_{(k)}$. They satisfy equations (2.1.33) and (2.1.34):

$$d\mu_{HOM(kK)}=-\left(\frac{\partial s}{\partial x_{(k)}}\right)_{T,\dots}dT+\sum_{l}\hat{\kappa}^{(l)ij}_{(kK)}d\hat{\varepsilon}^{(l)}_{ij}+\sum_{l}\hat{\omega}^{(l)ijk}_{(kK)}d\hat{\nabla}_k\hat{\varepsilon}^{(l)}_{ij}+\sum_{h}^{K-1}\Xi^{(kh)}dx_{(h)}+\sum_{h}^{K-1}\hat{l}^{i}_{(kKh)}d\hat{\nabla}_i x_{(h)} \tag{2.1.33}$$

and

$$d\hat{\mu}^{i}_{INH(kK)}=-\left(\frac{\partial s}{\partial\hat{\nabla}_i x_{(k)}}\right)_{T,\dots}dT+\sum_{l}\hat{\kappa}^{(l)rsi}_{\nabla(kK)}d\hat{\varepsilon}^{(l)}_{rs}+\sum_{l}\hat{\omega}^{(l)rspi}_{\nabla(kK)}d\hat{\nabla}_p\hat{\varepsilon}^{(l)}_{rs}+\sum_{h=1}^{K-1}\left[\hat{l}^{i}_{(kKh)}dx_{(h)}+\frac{\partial^2 a_F}{\partial\hat{\nabla}_i x_{(k)}\partial\hat{\nabla}_q x_{(h)}}d\hat{\nabla}_q x_{(h)}\right] \tag{2.1.34}$$

where $\Xi^{(kh)}$ and $\hat{l}^{i}_{(kKh)}$ are the components of coefficient tensors.

Because of the symmetry of the 2nd order derivatives of a_F, coefficients $\hat{\kappa}^{(l)ij}_{(kK)}$, $\hat{\omega}^{(l)ijk}_{(kK)}$, $\hat{\kappa}^{(l)rsi}_{\nabla(kK)}$, and $\hat{\omega}^{(l)rspi}_{\nabla(kK)}$ appear in both expressions of $\boldsymbol{\sigma}^{(l)}$ and $\mu_{(kK)}$. The coefficients $\hat{\kappa}^{(l)ij}_{(kK)}$, $\hat{\omega}^{(l)ijk}_{(kK)}$, $\hat{\kappa}^{(l)rsi}_{\nabla(kK)}$, and $\hat{\omega}^{(l)rspi}_{\nabla(kK)}$ are named coupling coefficients of the mechanical-chemical coupling effect.

2.2. Simplification and application

The general theory in Section 2.1 may be applied to a simplified solution system that represents the tin anode particle in Li-ion batteries, based on the assumptions below: (1) This solution system is a binary system with isotropic materials. (2) The temperature of the system is constant and evenly distributed. (3) The body force is neglected. (4) The materials of the system have no memory effect. (5) Only the interstitial diffusion of Li in the Sn anode is considered. (6) The electrochemical reaction of the Sn anode occurs only on the surface of the solution system. (7) The electrical potential is evenly distributed on the particle.

In the tin anode, Li atoms diffuse through the sites around Sn atoms. The solution system has two components, Li and Sn. We define three continuums: the Li continuum, Sn continuum and the mass center continuum. All three continuums have their corresponding deformed spaces. Li is defined as component 1 and Sn is defined as component 2. If there is no index of components marked in a function, that function is for the mass center continuum.

2.2.1. Mass conservation and kinematics

The boundary of the anode is determined by the boundary of the Sn continuum. For the convenience of setting the boundary conditions, we select the space of the Sn (component 2) as the reference space, of which the independent variables for the functions are (z^1, z^2, z^3, t), where z^i is the Eulerian coordinate of the mass center continuum and the Lagrangian coordinate of the Sn continuum.

Selecting the Sn space as the reference space means that $\boldsymbol{v}_{(2)}=\mathbf{0}$. The solution system is assumed to be a binary system. This system yields a simplified form of equation (2.1.4), as shown in equation (2.2.1) below,

$$\boldsymbol{J}_{(1)}=\rho_{(2)}\boldsymbol{v} \tag{2.2.1}$$

Substituting equation (2.2.1) into equation (2.1.7), with the assumption that there is no chemical reaction inside the system, yields the mass conservation equation:

$$\rho\dot{x}_{(1)}+\nabla\cdot\left(\rho_{(2)}\boldsymbol{v}\right)=0 \tag{2.2.2}$$

For the binary system, the molar fraction and the mass fraction are related by equation (2.2.3):

$$y'_{(1)}=\frac{M_{(2)}}{N_B M_{(1)}}\frac{x_{(1)}}{x_{(2)}} \tag{2.2.3}$$

where $y'_{(1)}$ is the molar fraction of the occupied Li sites, $M_{(1)}$ is the molar mass of Li, $M_{(2)}$ is the molar mass of Sn, and N_B is the average number of Li per Sn when the anode is fully lithiated.

We define the current density of lithiation as positive. The total current of the anode particle is as follows:

$$I=-F\int_A\frac{1}{M_{(1)}}\rho\boldsymbol{v}\cdot\boldsymbol{n}dA \tag{2.2.4}$$

where $\boldsymbol{n}$ is the normal vector of the surface.

Since only the interstitial diffusion is considered, we assume that the elastic strain and plastic strain rate of the anode particle are contributed from the Sn atoms, as shown in equations (2.2.5) and (2.2.6):

$$\boldsymbol{\varepsilon}^{(e)}=\boldsymbol{\varepsilon}^{(e)}_{(2)} \tag{2.2.5}$$

and

$$\dot{\boldsymbol{e}}^{(p)}=\dot{\boldsymbol{e}}^{(p)}_{(2)} \tag{2.2.6}$$

where $\boldsymbol{\varepsilon}^{(e)}$ is the elastic strain of the mass center continuum, $\boldsymbol{\varepsilon}^{(e)}_{(2)}$ is the elastic strain of the Sn continuum, $\dot{\boldsymbol{e}}^{(p)}$ is the plastic strain rate of the mass center continuum, and $\dot{\boldsymbol{e}}^{(p)}_{(2)}$ is the plastic strain rate of the Sn continuum. In addition, we assume that the Sn continuum has only the elastic deformation and the plastic deformation. Since the reference space is the Lagrangian space of the Sn continuum, the additive decomposition of strain component demonstrated by equation (2.1.11) yields three kinematic relations for the Sn continuum, as shown in equations (2.2.7), (2.2.8), and (2.2.9):

$$\varepsilon_{(2)ij} = \varepsilon^{(e)}_{(2)ij} + \varepsilon^{(p)}_{(2)ij} \tag{2.2.7}$$

$$\dot{e}_{(2)ij} = \frac{1}{2}\left(\nabla_i v^L_{(2)j} + \nabla_j v^L_{(2)i}\right) = \frac{\partial \varepsilon_{(2)ij}}{\partial t} = \frac{1}{2}\frac{\partial g_{(2)ij}}{\partial t} \tag{2.2.8}$$

$$\dot{e}^{(p)}_{(2)ij} = \frac{\partial \varepsilon^{(p)}_{(2)ij}}{\partial t} \tag{2.2.9}$$

where $\varepsilon_{(2)ij}$ is the covariant component for the total strain of the Sn continuum, $\varepsilon^{(e)}_{(2)ij}$ is the covariant component for the elastic strain of the Sn continuum, $\varepsilon^{(p)}_{(2)ij}$ is the covariant component for the plastic strain of the Sn continuum, $\dot{e}_{(2)ij}$ is the covariant component for the total strain rate of the Sn continuum, $v^L_{(2)j}$ is the covariant component for the velocity of the Sn continuum relative to the lab space, $g_{(2)ij}$ is the metric of the Sn space, and $\dot{e}^{(p)}_{(2)ij}$ is the covariant component for the plastic strain rate of the Sn continuum. By substituting equations (2.2.5), (2.2.6), and (2.2.7) into equation (2.2.8), we have the relations between the deformation of the mass center continuum and the deformation of the Sn continuum as shown below,

$$\frac{\partial \varepsilon^{(e)}_{ij}}{\partial t} + \dot{e}^{(p)}_{ij} = \frac{1}{2}\left(\nabla_i v^L_{(2)j} + \nabla_j v^L_{(2)i}\right) \tag{2.2.10}$$

and

$$\frac{\partial \varepsilon^{(e)}_{ij}}{\partial t} + \dot{e}^{(p)}_{ij} = \frac{1}{2}\frac{\partial g_{(2)ij}}{\partial t} \tag{2.2.11}$$

The constitutive equations for the finite deformation should be formulated based on rate functions. For the mass center continuum, the elastic strain rate is connected to its elastic strain by equation (2.2.12) (Sedov, 1997):

$$\dot{e}^{(e)}_{ij} = \frac{\partial \varepsilon^{(e)}_{ij}}{\partial t} + \varepsilon^{(e)}_{kj}\frac{\partial v^k}{\partial z^i} + \varepsilon^{(e)}_{il}\frac{\partial v^l}{\partial z^j} + v^k\frac{\partial \varepsilon^{(e)}_{ij}}{\partial z^k} \tag{2.2.12}$$

where $\dot{e}^{(e)}_{ij}$ is the covariant component for the elastic strain rate of the mass center continuum and v^i is the contravariant component of the mass center velocity. The total strain rate of the mass center continuum depends on the mass center velocity relative to the lab space, which is equal to the mass center velocity relative to the reference space plus the velocity of the reference space relative to the lab space. It yields equation (2.2.13):

$$\dot{\boldsymbol{e}} = \frac{1}{2}\left[\nabla \boldsymbol{v} + (\nabla \boldsymbol{v})^T\right] + \frac{1}{2}\left[\nabla \boldsymbol{v}^L_{(2)} + \left(\nabla \boldsymbol{v}^L_{(2)}\right)^T\right] \tag{2.2.13}$$

where the first part $\frac{1}{2}\left[\nabla \boldsymbol{v} + (\nabla \boldsymbol{v})^T\right]$ is the mass center strain rate induced by diffusion, called diffusion-induced creep rate, and the second part is the mass center strain rate induced by the Sn continuum.

2.2.2. Dissipation models of non-equilibrium process

Equation (2.1.24) for the entropy production rate reveals 4 parts for the dissipation of the solution system: thermal, mechanical, diffusional, and chemical reactions. For the system with an evenly distributed temperature, thermal dissipation is canceled. The other three dissipations are modeled in this section.

Because there is no memory effect, $\boldsymbol{\sigma}^{(p)} = \mathbf{0}$. The elastic stress is marked as $\boldsymbol{\sigma}$. It yields as follows:

$$\boldsymbol{\tau}^{(p)} = \boldsymbol{p} = \boldsymbol{\tau}^{(e)} + \boldsymbol{\sigma} \tag{2.2.14}$$

The mechanical dissipation is assumed to be related to $\dot{\boldsymbol{e}}^{(p)}$ and $\dot{\boldsymbol{e}}^{(e)}$. Substituting equation (2.2.14) into equation (2.1.24) yields as follows:

$$T\theta_M = \boldsymbol{\sigma} : \dot{\boldsymbol{e}}^{(p)} + \boldsymbol{\tau}^{(e)} : \left(\dot{\boldsymbol{e}}^{(e)} + \dot{\boldsymbol{e}}^{(p)}\right) \tag{2.2.15}$$

where θ_M is the mechanical entropy production rate. For the term $\boldsymbol{\sigma} : \dot{\boldsymbol{e}}^{(p)}$, we describe the plastic strain rate with the classic form of the plasticity flow as follows:

$$\dot{\boldsymbol{e}}^{(p)} = 2\lambda^{(P)}\boldsymbol{S}^{(e)} \tag{2.2.16}$$

where $\lambda^{(P)}$ is the coefficient of the plastic strain rate, which is called the plasticity rate in this paper, and $\boldsymbol{S}^{(e)}$ is the deviatoric tensor of $\boldsymbol{\sigma}$.

Substituting equation (2.2.16) into equation (2.2.15) yields as follows:

$$T\theta_M = 2\lambda^{(P)}\psi + \boldsymbol{\tau}^{(e)} : \left(\dot{\boldsymbol{e}}^{(e)} + \dot{\boldsymbol{e}}^{(p)}\right) \tag{2.2.17}$$

with

$$\psi = \boldsymbol{\sigma} : \boldsymbol{S}^{(e)} = \boldsymbol{S}^{(e)} : \boldsymbol{S}^{(e)} \tag{2.2.18}$$

Equation (2.2.17) reveals that ψ may be considered as a generalized force of the generalized flow $\lambda^{(P)}$. The function $\lambda^{(P)} = \lambda^{(P)}(\psi)$ is modeled by introducing the transition-state theory into the plasticity. Atoms should pass the transition state for causing plastic deformation. This mechanism is named kinetic plasticity and is shown below:

$$\lambda^{(P)} = \lambda^{(P)+} - \lambda^{(P)-} \tag{2.2.19}$$

$$\lambda^{(P)\pm} = C^{(p)\pm}\exp\left(-\frac{E^{(p)\pm}_A}{RT}\right) \tag{2.2.20}$$

$$E^{(p)+}_A = a^{(p)}K_\psi\psi + E^{(p)}_{A0} \tag{2.2.21}$$

$$E^{(p)-}_A = \left(a^{(p)} + 1\right)K_\psi\psi + E^{(p)}_{A0} \tag{2.2.22}$$

where $\lambda^{(P)\pm}$ is forward/backward plasticity rate, $C^{(p)\pm}$ are pre-exponential factors of the forward/backward plasticity rate, $a^{(p)}$ is a symmetry coefficient of the plasticity rate, K_ψ is the stress-activation energy coefficient, and $E^{(p)}_{A0}$ is the reference activation energy of the plasticity rate.

During the plastic deformation, when some atoms are passing the transition state from the old state to the new one, that event corresponds to the forward plasticity rate. Additionally, some atoms may go back to the old state from the new one. This event corresponds to the backward plasticity rate. The net plasticity rate is the difference between the forward plasticity rate and the backward plasticity rate. The probability of passing the transition state obeys the Boltzmann distribution with forward/backward activation energy. The forward/backward activation energy is assumed to be linear with the ψ.

The dissipation stress $\boldsymbol{\tau}^{(e)}$ in equation (2.2.17) is known as viscous stress. We assume it as follows:

$$\boldsymbol{\tau}^{(e)} = \boldsymbol{\eta}^{(e)} : \dot{\boldsymbol{e}}^{(e)} + \boldsymbol{\eta}^{(p)} : \dot{\boldsymbol{e}}^{(p)} \tag{2.2.23}$$

where $\boldsymbol{\eta}^{(e)}$ and $\boldsymbol{\eta}^{(p)}$ are the coefficients of viscosity related to elastic strain rate and plastic strain rate respectively. The existence of viscosities makes the non-equilibrium process stable. Solving the equations of the system may give divergent results if the coefficients of the viscosity are not carefully chosen.

The material is assumed to be isotropic. Hence, $\boldsymbol{\eta}^{(e)}$ and $\boldsymbol{\eta}^{(p)}$ have simplified forms related to the metric as follows:

$$\eta^{(e)ijkl} = \eta^{(e)}_H g^{ij}_{(2)}g^{kl}_{(2)} + \eta^{(e)}_D g^{ik}_{(2)}g^{jl}_{(2)} + \eta^{(e)}_D g^{il}_{(2)}g^{jk}_{(2)} \tag{2.2.24}$$

and

$$\eta^{(p)ijkl} = \eta^{(p)}_H g^{ij}_{(2)}g^{kl}_{(2)} + \eta^{(p)}_D g^{ik}_{(2)}g^{jl}_{(2)} + \eta^{(p)}_D g^{il}_{(2)}g^{jk}_{(2)} \tag{2.2.25}$$

where $g^{ij}_{(2)}$ is the contravariant component of the metric tensor for the reference space, and $\eta^{(e)}_H$, $\eta^{(e)}_D$, $\eta^{(p)}_H$, and $\eta^{(p)}_D$ are material parameters.

Substituting equation (2.2.16) into equation (2.2.23) yields a simplified form of $\boldsymbol{\tau}^{(e)}$ by cancelling the $\eta^{(p)}_H$:

$$\boldsymbol{\tau}^{(e)} = \boldsymbol{\eta}^{(e)} : \dot{\boldsymbol{e}}^{(e)} + 4\eta^{(p)}_D \dot{\lambda}^{(P)} \boldsymbol{S}^{(e)} \tag{2.2.26}$$

For isotropic materials, the parameters are zero for the 1st and the 3rd order coefficient tensors (Sedov, 1997). Hence, for the diffusional dissipation, there should be no coupling between $\boldsymbol{J}_{(1)}$ and $A^{(j)}_C$, or between $\boldsymbol{J}_{(1)}$ and $\dot{\boldsymbol{e}}^{(l)}$. The body force is neglected. It yields as follows:

$$T\theta_{(1)} = -\boldsymbol{J}_{(1)} \cdot \nabla \mu_{(12)} \tag{2.2.27}$$

where $\theta_{(1)}$ is the diffusional entropy production rate of the simplified system. The relation between $\boldsymbol{J}_{(1)}$ and $\nabla\mu_{(12)}$ is expressed as follow:

$$J^i_{(1)} = -\frac{L}{T} g^{ij}_{(2)} \nabla_j \mu_{(12)} \tag{2.2.28}$$

with

$$L = L_0 f_L(x_{(1)}) \tag{2.2.29}$$

where $J^i_{(1)}$ is the contravariant component of Li flux, L is the thermodynamic coefficient of diffusion, and L_0 is the reference thermodynamic coefficient of diffusion. Coefficient L depends on the mass fraction of Li. According to equations (2.1.4) and (2.1.5), $\boldsymbol{J}_{(1)}$ is zero when $x_{(1)}$ is zero. Hence, L should be zero when $x_{(1)}$ is zero. Moreover, we assume that L is zero when the anode is fully lithiated.

We set lithiation as the forward reaction. The chemical reaction on the surface is as follows:

$$Li^+ + e^- \leftrightarrow Li \tag{2.2.30}$$

where Li^+ is the Li-ion from the electrolyte and e^- is the electron from the anode. The surface region may not be considered as the binary system since there are more than two components on the surface. We define the Li-ion as component 3.

The molar electrochemical potential of the Li-ion in the electrolyte is expressed as follows:

$$\mu_{(30)M} = \mu_{(32)} M_{(1)} + F\phi \tag{2.2.31}$$

where $\mu_{(30)M}$ is the molar electrochemical potential of the Li-ion in the electrolyte, F is the Faraday's constant, and ϕ is the electrical potential based on the location of Li-ion. If the diffusivity of the Li-ion in the electrolyte is much higher than the diffusivity of Li in the anode, we may consider the electrolyte to always be in equilibrium relative to the anode. Hence, $\mu_{(30)M}$ should be constant and evenly distributed in the electrolyte. Substituting equation (2.2.31) into equation (2.1.28) yields as follows:

$$A_{CM} = \mu_{(30)M} - \left(F\phi + \mu_{(12)} M_{(1)}\right) \tag{2.2.32}$$

where A_{CM} is the molar chemical affinity.

We define the molar reaction rate J_M with $J_M = J/M_{(1)}$. Based on the transition-state theory, the function $J_M = J_M(A_{CM})$ is modeled by equations (2.2.33), (2.2.34), (2.2.35), and (2.2.36):

$$J_M = J^+_M - J^-_M \tag{2.2.33}$$

$$J^{\pm}_M = C^{(R)\pm} \exp\left(-\frac{E^{(R)\pm}_A}{RT}\right) \tag{2.2.34}$$

$$E^{(R)+}_A = a^{(R)} A_{CM} + E^{(R)}_{A0} \tag{2.2.35}$$

$$E^{(R)-}_A = \left(a^{(R)} + 1\right) A_{CM} + E^{(R)}_{A0} \tag{2.2.36}$$

where $J^{\pm}_M$ is the forward/backward molar reaction rate, $C^{(R)\pm}$ is pre-exponential factors of the forward/backward molar reaction rate, $a^{(R)}$ is the symmetry coefficient of the molar reaction rate, and $E^{(R)}_{A0}$ is the reference activation energy of the molar reaction rate.

2.2.3. Models of state functions

For isotropic materials, $\hat{C}^{ijkl}_{\rho}$ and $\hat{\kappa}^{(l)ij}_{(kK)}$ have simplified forms related to the metric tensor. It yields as follows:

$$\hat{C}^{ijkl}_{\rho} = \lambda_\rho \hat{g}^{ij} \hat{g}^{kl} + G_\rho \hat{g}^{ik} \hat{g}^{jl} + G_\rho \hat{g}^{il} \hat{g}^{jk} \tag{2.2.37}$$

and

$$\hat{\kappa}^{ij}_{(12)} = \kappa \hat{g}^{ij} \tag{2.2.38}$$

where κ is related to the expansion ratio defined by $\alpha_{ij} = \alpha \hat{g}_{ij} = \left(\frac{\partial \hat{\varepsilon}^{(e)}_{ij}}{\partial x_{(1)}}\right)_{\frac{\sigma_{HOM}}{\rho}}$. The chain rule $\frac{\partial}{\partial x_{(1)}}\left(\frac{\hat{\sigma}^{ij}_{HOM}}{\rho}\right)_{\hat{\varepsilon}^{(e)}_{kl}} = -\frac{\partial}{\partial \hat{\varepsilon}^{(e)}_{kl}}\left(\frac{\hat{\sigma}^{ij}_{HOM}}{\rho}\right)_{x_{(1)}} \left(\frac{\partial \hat{\varepsilon}^{(e)}_{kl}}{\partial x_{(1)}}\right)_{\frac{\sigma_{HOM}}{\rho}}$ yields the connection between κ and α:

$$\kappa = -(3\lambda_\rho + 2G_\rho)\alpha \tag{2.2.39}$$

where α is related to the partial molar volume V_{PM} by

$$\alpha = \frac{1}{3} \frac{\rho V_{PM}}{M_{(1)} x_{(2)}} \tag{2.2.40}$$

Since for isotropic materials, the parameters are zero for the 3rd and 5th order coefficient tensors (Sedov, 1997), we can cancel the $\hat{C}^{(l)ijrsp}_{\rho\nabla}$, $\hat{\kappa}^{(l)ijq}_{\nabla(kK)}$, $\hat{\Lambda}^{(l)ijklm}$, $\hat{\omega}^{(l)ijk}_{(kK)}$, and $\hat{\chi}^{(l)ijk}$ in equations (2.1.31) and (2.1.32). There are 15 independent components for 6th order isotropic tensors (Kearsley and Fong, 1975). With considering the symmetries of stress tensor and strain tensor, the number of the independent components for $\boldsymbol{\Lambda}_\nabla$ decreases to six: $\Lambda_{\nabla(1)} \hat{g}^{ij} \hat{g}^{kp} \hat{g}^{lm}$, $\Lambda_{\nabla(2)} \hat{g}^{ij} \hat{g}^{kl} \hat{g}^{mp}$, $\Lambda_{\nabla(3)} \hat{g}^{ik} \hat{g}^{jl} \hat{g}^{mp}$, $\Lambda_{\nabla(4)} \hat{g}^{ik} \hat{g}^{jp} \hat{g}^{lm}$, $\Lambda_{\nabla(5)} \hat{g}^{il} \hat{g}^{jm} \hat{g}^{kp}$, and $\Lambda_{\nabla(6)} \hat{g}^{il} \hat{g}^{jp} \hat{g}^{km}$. For simplicity, $\hat{\Lambda}^{ijklmp}_{\nabla}$ and $\hat{\omega}^{ijkq}_{\nabla(12)}$ are expressed in only one component of them. Hence, we assume

$$\hat{\Lambda}^{ijklmp}_{\nabla} = \Lambda_\nabla \hat{g}^{ij} \hat{g}^{kp} \hat{g}^{lm} \tag{2.2.41}$$

$$\hat{\omega}^{ijkq}_{\nabla(12)} = \omega_l \hat{g}^{ij} \hat{g}^{kq} \tag{2.2.42}$$

By substituting equations (2.2.41) and (2.2.42) into equations (2.1.31) and (2.1.32), equation (2.1.18) yields the model of the objective elastic stress rate $\dot{\boldsymbol{\Omega}}$ as shown below,

$$\dot{\Omega}^{ij} = C^{ijkl}_{\rho} \rho \dot{e}^{(e)}_{kl} - \sigma^{ij} \dot{e}^m_m + \kappa g^{ij}_{(2)} \rho \dot{x}_{(1)} + 2\rho\left(\nabla^2 f_{\varepsilon x}\right)\dot{e}^{ij} - \rho g^{ij}_{(2)} \times \frac{d\left(\nabla^2 f_{\varepsilon x}\right)}{dt} \tag{2.2.43}$$

with

$$f_{\varepsilon x} = \Lambda_\nabla \varepsilon^{(e)m}_{\ \ m} + \omega_l x_{(1)} \tag{2.2.44}$$

The relation between the objective elastic stress rate and the elastic stress is as follows (Sedov, 1997):

$$\dot{\Omega}^{ij} = \frac{\partial \sigma^{ij}}{\partial t} - \sigma^{pj} \frac{\partial v^i}{\partial z^p} - \sigma^{iq} \frac{\partial v^j}{\partial z^q} + v^k \frac{\partial \sigma^{ij}}{\partial z^k} \tag{2.2.45}$$

The relative chemical potential $\mu_{(12)}$ is divided into an ideal part and an excess part. The entropy of the ideal part obeys the ideal solution model (DeHoff, 2006). We assume that specific entropy s

is independent of $\nabla x_{(1)}$ and $\nabla \varepsilon^{(l)}$. Hence, combining equations (2.1.21), (2.1.29), (2.1.30), (2.1.31), (2.1.33), and (2.1.34) yields the relative chemical potential model below. The derivation steps are shown in Appendix A4.

$$\frac{\partial \mu_{EX(12)}}{\partial t} + v^k \frac{\partial \mu_{EX(12)}}{\partial z^k} = K_D \dot{e}^{(e)m}_{\ \ m} + h\dot{x}_{(1)} \tag{2.2.46}$$

$$\mu_{(12)} = RT\left[\frac{1}{M_{(1)}}\ln\frac{y'_{(1)}}{y'_{(2)}} - \frac{N_B}{M_{(2)}}\ln y'_{(2)}\right] - \omega_I \nabla^2 \varepsilon^{(e)m}_{\ \ m} - K_{(12)}\nabla^2 x_{(1)} + \mu_{EX(12)} \tag{2.2.47}$$

$$K_D = \kappa - \frac{T}{x_{(2)}}\gamma \tag{2.2.48}$$

$$\gamma = -(3\lambda_\rho + 2G_\rho)\alpha_T \tag{2.2.49}$$

where $\mu_{EX(12)}$ is the excess relative chemical potential, h is the material parameter of the relative chemical potential, calculated by $h = k_{hRT}RT/M_{(2)}$, R is gas constant, $y'_{(2)}$ is the molar fraction of unoccupied Li sites, $K_{(12)}$ is the material parameter of the relative chemical potential, and α_T is the thermal expansion ratio.

2.3. Numerical simulation

2.3.1. Transformation of equations and numerical method

For the convenience of simulating Sn anode particles, we transform the following equations into conducive forms for linearization: equation (2.2.2) for mass conservation, the momentum equation (2.1.12), the diffusion equation (2.2.28), equation (2.2.20) for the plasticity rate, equation (2.2.34) for the chemical reaction rate, and equation (2.2.47) for the relative chemical potential. The derivation steps of the transformation are shown in Appendix A5. The transformed equations are shown below:

The equation for mass conservation is transformed into:

$$\rho\dot{x}_{(1)} - \frac{L_0 R}{M_{(1)}}\left[f_{L1}\nabla^2 x_{(1)} + g^{ij}_{(2)}(\nabla_i f_{L1})(\nabla_j x_{(1)})\right] - \frac{L_0}{T}\left[f_L\nabla^2\mu_{IE(12)} + g^{ij}_{(2)}(\nabla_i f_L)\left(\nabla_j \mu_{IE(12)}\right)\right] = 0 \tag{2.3.1}$$

$$f_L(x_{(1)}) = A_L(x_{(1)})^{N_1}(1-x_{(1)})^{N_2}\left[1 - \left(\frac{M_{(2)}}{N_B M_{(1)}} + 1\right)x_{(1)}\right]^{N_3} \tag{2.3.2}$$

$$f_{L1}(x_{(1)}) = A_L(x_{(1)})^{N_1-1}(1-x_{(1)})^{N_2-1}\left[1 - \left(\frac{M_{(2)}}{N_B M_{(1)}} + 1\right)x_{(1)}\right]^{N_3-1} \tag{2.3.3}$$

where $\mu_{IE(12)}$ is inhomogeneous and an excess part of the relative chemical potential and A_L, N_1, N_2, N_3 are material parameters related to f_L.

The momentum equation is transformed into:

$$\nabla_j p^{ij} = \rho\left(\frac{\partial v^i}{\partial t} + v^k\nabla_k v^i + \frac{\partial v^L_{(2)j} g^{ij}_{(2)}}{\partial t} + v^L_{(2)j}\nabla_k v^L_{(2)m} g^{kj}_{(2)} g^{mi}_{(2)}\right) \tag{2.3.4}$$

$$p^{ij} = \sigma^{ij} + \left(\eta_H g^{ij}_{(2)} g^{kl}_{(2)} + 2\eta_D g^{ik}_{(2)} g^{jl}_{(2)}\right)\dot{e}^{(e)}_{kl} + 4\eta^{(p)}_D \lambda^{(P)} S^{(e)ij} \tag{2.3.5}$$

The diffusion equation is transformed into:

$$\rho_{(2)} v^i = -L_0 g^{ij}_{(2)}\left[\frac{R}{M_{(1)}} f_{L1}\nabla_j x_{(1)} + \frac{f_L}{T}\nabla_j \mu_{IE(12)}\right] \tag{2.3.6}$$

The equation for the plasticity rate is transformed into:

$$\frac{\partial \lambda^{(P)+}}{\partial t} = -\frac{a^{(p)} K_\psi}{RT}\lambda^{(P)+}\frac{\partial \psi}{\partial t} \tag{2.3.7}$$

$$\frac{\partial \lambda^{(P)-}}{\partial t} = -\frac{(a^{(p)}+1) K_\psi}{RT}\lambda^{(P)-}\frac{\partial \psi}{\partial t} \tag{2.3.8}$$

$$\frac{\partial \psi}{\partial t} = 2\left(S^{(e)}_{ij}\frac{\partial \sigma^{ij}}{\partial t} + S^{(e)ij}\sigma^{uv}\frac{\partial g_{(2)ui}}{\partial t} g_{(2)vj}\right) \tag{2.3.9}$$

The equation for the chemical reaction rate is transformed into:

$$\frac{\partial J^+_M}{\partial t} = -\frac{a^{(R)}}{RT} J^+_M \frac{\partial A_{CM}}{\partial t} \tag{2.3.10}$$

$$\frac{\partial J^-_M}{\partial t} = -\frac{a^{(R)}+1}{RT} J^-_M \frac{\partial A_{CM}}{\partial t} \tag{2.3.11}$$

$$\frac{\partial A_{CM}}{\partial t} = -\left[F\frac{\partial \phi}{\partial t} + M_{(1)}\left(\frac{\partial \mu_{HL(12)}}{\partial x_{(1)}}\frac{\partial x_{(1)}}{\partial t} + \frac{\partial \mu_{IE(12)}}{\partial t}\right)\right] \tag{2.3.12}$$

$$\frac{\partial \mu_{HL(12)}}{\partial x_{(1)}} = \frac{RTN_B}{M_{(2)}}\left[\frac{k}{x_{(1)}} - \frac{1}{x_{(2)}} + \frac{(k+1)^2}{1-(k+1)x_{(1)}}\right] \tag{2.3.13}$$

$$k = \frac{M_{(2)}}{N_B M_{(1)}} \tag{2.3.14}$$

where $\mu_{HL(12)}$ is the homogeneous-logarithm relative chemical potential.

The equation for the relative chemical potential is transformed into:

$$\mu_{IE(12)} = -\omega_I \nabla^2 \varepsilon^{(e)m}_{\ \ m} - K_{(12)}\nabla^2 x_{(1)} + \mu_{EX(12)} \tag{2.3.15}$$

For the numerical simulations, we have equations (2.2.43), (2.2.39), (2.2.40), (2.2.44), (2.3.4), (2.3.5), (2.2.13), (2.2.19), (2.3.7), (2.3.8), (2.3.9), (2.2.10), (2.3.1), (2.3.2), (2.3.3), (2.1.8), (2.2.45), (2.2.12), (2.3.6), (2.2.46), (2.2.48), (2.3.15), (2.2.11), and (2.1.5). To make the number of variables equal to the number of equations, the four additional equations shown below are necessary:

$$\frac{\partial \rho_{(2)}}{\partial t} + \rho_{(2)}\nabla\cdot \boldsymbol{v}^{(L)}_{(2)} = 0 \tag{2.3.16}$$

$$\left[g_{(2)ij}\right] = \left[g^{ij}_{(2)}\right]^{-1} \tag{2.3.17}$$

$$\lambda_\rho = \lambda/\rho \tag{2.3.18}$$

$$G_\rho = G/\rho \tag{2.3.19}$$

where λ and G are Lame constants.

We have 28 equations above with 28 variables below to numerically solve the non-equilibrium process of the Sn anode particle, namely, $\dot{\boldsymbol{\Omega}}$, κ, α, f_{ex}, $\boldsymbol{v}^L_{(2)}$, $\boldsymbol{p}$, $\dot{\boldsymbol{e}}$, $\lambda^{(P)}$, $\lambda^{(P)+}$, $\lambda^{(P)-}$, ψ, $\dot{\boldsymbol{e}}^{(e)}$, $\dot{x}_{(1)}$, f_L, f_{L1}, $x_{(1)}$, $\boldsymbol{\sigma}$, $\boldsymbol{\varepsilon}^{(e)}$, $\boldsymbol{v}$, $\mu_{EX(12)}$, K_D, $\mu_{IE(12)}$, $g_{(2)ij}$, ρ, $\rho_{(2)}$, $g^{ij}_{(2)}$, λ_ρ, and G_ρ.

We apply the finite difference method coded with MATLAB to solve the equation set of the solution system numerically. We use a mesh generator program from Persson and Strang (2004) to generate the grid of the discretized anode particle. The derivative matrices of the finite difference are built based on the method from Perrone and Kao (1975). We use the implicit method of finite difference scheme to keep the system numerically stable and convergent. System equations are solved in every time step. The equations of the solution system are nonlinear. To reduce the computational cost, Newton's iteration is avoided at every time step. The equations are simply linearized by setting the variables as

input coefficients for every time step if the variables are integrated over time in the simulation.

2.3.2. Geometry and material parameters of the particle

Fig. 1a shows the initial spherical cap geometry of the anode particle bonded on a flat current collector, based on the size of the Sn particle observed in Takeuchi (2016). To prevent stress concentration, the fillet is set on the connection between the current collector and the particle. We use the cylindrical coordinate frame (z^1, z^2, z^3) on the initial Sn space, where z^2 is the angle coordinate. The origin of the coordinate frame coincides with the spherical center of the spherical cap.

For simplicity, the numerical simulation of phase separation and the inhomogeneous stress are neglected in this paper. Hence we set $\Lambda_\nabla = 0$, $\omega_I = 0$, $K_{(12)} = 0$. Other material parameters used for the computation are shown in Table 1. $\eta_H^{(e)}$, $\eta_D^{(e)}$ and $\eta_D^{(p)}$ are assigned by referring the viscosity of glass at transition state (Zheng and Mauro, 2017). Because the stiffness of electrodes may change during charging/discharging (Maxisch and Ceder, 2006; Stournara et al., 2012; Shenoy et al., 2010), the Lame constants are multiplied by factors $\lambda = k_{\lambda G}\lambda_0$ and $G = k_{\lambda G}G_0$, where λ_0 and G_0 are Lame constants of pure Sn (Qi et al., 2014). The partial molar volume V_{PM} is determined by $V_{PM} = \frac{M_{(2)}R_V}{\rho_0 N_B}$, where R_V is the ratio of the expanded volume of the anode particle after it is fully lithiated by the ideal process that is stress-free and possesses quasi-equilibrium, and ρ_0 is the density of pure Sn. To save on the computation cost, we set $R_V = 1$ which is half of the ratio of a real Sn anode (Qi et al., 2014).

The thermodynamic coefficient of diffusion L in equation (2.2.28) can be connected to the diffusivity D in Fick's law. With the values of N_1, N_2, and N_3 in Table 1, equation (2.2.29) and equation (2.3.2) yield the curve of L. Comparing equation (2.2.28) with Fick's 1st law yields the corresponding D of L as shown in Fig. 1b. The derivation steps are shown in Appendix A6. The shape of D is basically consistent with the results in Ding (2009). The value of D agrees the range between 8×10^{-20} m^2/s and 5.9×10^{-11} m^2/s mentioned in Shi et al. (2016).

2.3.3. Boundary conditions, initial conditions and deformation

Due to the symmetry, we calculate the right half of the particle. In Fig. 1a, the segment from point A to point C is designated the bottom, and the segment from point C to point B is called an arc.

The mechanical boundary condition is

$$k_{BAM}^{(i)} p^{ij} n_j + \eta_{BA}\left(1 - k_{BAM}^{(i)}\right) v_{(2)j}^{L} g_{(2)}^{ij} = 0 \tag{2.3.20}$$

with

$$k_{BAM}^{(i)} = \frac{2}{\pi}\arctan\left\{(l)^{a_{(i)}}\left[1-(l)^{b_{(i)}}\right]^{-c_{(i)}}\right\} \tag{2.3.21}$$

where $k_{BAM}^{(i)}$ is the bottom-arc mixing coefficient for the mechanical boundary condition. $k_{BAM}^{(i)}$ helps to prevent singularity by making the mechanical boundary condition change continuously from the bottom to the arc. $k_{BAM}^{(i)}$ is a monotone-increasing function of l with value settings of $a_{(i)}$, $b_{(i)}$ and $c_{(i)}$. l represents the location along the boundary passing through points A, C, D, and B in Fig. 1a. $l = 0$ at point A and $l = 1$ at point B. For both $i = 1$ and $i = 3$, we set $k_{BAM}^{(i)} = 0.1$ at point C, $k_{BAM}^{(i)} = 0.9$ at point D, and $k_{BAM}^{(i)} = 0.5$ at the midpoint of the boundary segment between points C point D in Fig. 1a.

The kinetic boundary condition is composed of the following equations: equation (2.1.7) for mass conservation, equations (2.2.33), (2.3.10), (2.3.11), (2.3.12), and (2.3.13) for chemical reaction, and equation (2.2.4) for the total electric current. The reaction region is very thin compared to the whole particle. The mass conservation equation can be simplified as

$$\rho v \cdot n = -J_M M_{(1)} h_R \tag{2.3.22}$$

where h_R is the thickness of the reaction region. In Table 1, h_R is assigned by referring the thickness of electrical double layer (Marcicki et al., 2014).

Ideally, the chemical affinity on the segment will be zero where the particle contacts the current collector; i.e., only the surface where the particle contacts the electrolyte has the chemical reaction. Like the mechanical boundary condition, to avoid singularity, we set the kinetic boundary condition changes continuously along the surface. A coefficient k_{BAk} with the same mathematical form as equation (2.3.21) is multiplied on the right side of equation (2.3.12).

The surface area of the particle changes during (de)lithiation. Based on the particle symmetry with respect to z^2, the dA of the integral in equation (2.2.4) changes according to equation (2.3.23) as shown below:

$$\left(\frac{dA}{dA_0}\right)^2 = \frac{g_{(2)11} - 2g_{(2)13}\left(z^1/z^3\right) + g_{(2)33}\left(z^1/z^3\right)^2}{1+\left(z^1/z^3\right)^2}\left[\frac{g_{(2)22}}{\left(z^1\right)^2}\right] \tag{2.3.23}$$

The derivation steps are shown in Appendix A7. With the kinetic boundary condition, J_M, J_M^+, J_M^-, A_{CM}, $\mu_{HL(12)}$, and ϕ are added into the equation set for the anode particle in the galvanostatic mode of lithiation.

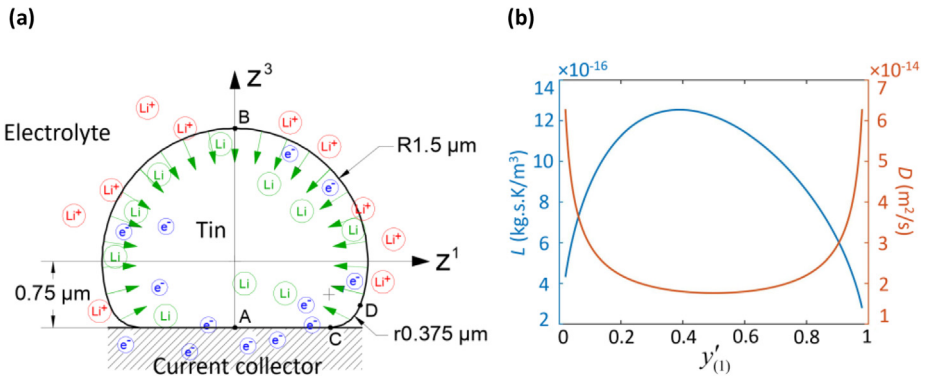

Fig. 1. (a) A representative Sn anode particle used in the simulation. Initially, the particle is a spherical cap with a fillet. The radius of the spherical cap is 1.5 μm. The radius of the fillet between points C and D is 0.375 μm. The distance between the spherical center and the current collector is 0.75 μm. (b) The curves of the thermodynamic coefficient of diffusion L and the diffusivity D serve as functions of the molar fraction of occupied Li sites $y'_{(1)}$.

Table 1
Material parameters used in the simulation.

Parameter	Unit	Value	Ref.	Parameter	Unit	Value	Ref.
$M_{(1)}$	kg/mol	6.94×10^{-3}	Lide (2005)	T	K	300	
$M_{(2)}$	kg/mol	0.119	Lide (2005)	L_0	kg s K/m^3	1×10^{-15}[b]	
N_B	–	4.4	Takeuchi (2016)	R_V	–	1	Qi et al. (2014)
ρ_0	kg/m^3	7.265×10^3	Lide (2005)	N_1	–	0.5[b]	
λ_0	GPa	40.4384	Qi et al. (2014)	N_2	–	1[b]	
G_0	GPa	19.0299	Qi et al. (2014)	N_3	–	0.5[b]	
α_T	K^{-1}	2.2×10^{-5}	Lide (2005)	$k_{\lambda G}$	–	0.7	Stournara et al. (2012)
$\eta_H^{(e)}$	GPa s	2000	Zheng and Mauro (2017)	k_{hRT}	–	4000[c]	
$\eta_D^{(e)}$	GPa s	1000	Zheng and Mauro (2017)	h_R	nm	1.05	Marcicki et al. (2014)
$\eta_D^{(p)}$	GPa s	1000	Zheng and Mauro (2017)	ϕ_0	V	1[c]	
$\lambda_0^{(p)}$	(Pa s)$^{-1}$	1×10^{-14}[a]		$\Delta\phi_{R1C}$	V	−0.1[c]	
$a^{(p)}$	–	−0.5		Δt_I	s	5	
K_ψ	J/Pa^2	3×10^{-10}[a]		$y'_{(1)0}$	–	5×10^{-4}	
$a^{(R)}$	–	−0.5		J_{M0}	mol/(m^3 s)	5.9011×10^3 [c]	

[a] Estimated value fit to results shown in Fig. 3.
[b] Estimated value fit to curves shown in Fig. 1b.
[c] Estimated value fit to results shown in Fig. 7.

To make the simulation more stable, we set the total electric current in the collector changes continuously between zero and the maximum. The duration of the change is Δt_I. When the time is zero, the nonzero initial conditions of the system are

$$y'_{(1)} = y'_{(1)0} \tag{2.3.24}$$

$$\lambda^{(P)+} = \lambda^{(P)-} = \lambda_0^{(p)} \tag{2.3.25}$$

$$J_M^+ = J_M^- = J_{M0} \tag{2.3.26}$$

$$\phi = \phi_0 \tag{2.3.27}$$

$$g_{(2)ij} = \delta_{ij} \tag{2.3.28}$$

$$\rho_{(2)} = \rho_0 \tag{2.3.29}$$

where $y'_{(1)0}$ is used for avoiding the negative infinity of the relative chemical potential, the reference chemical reaction rate J_{M0} can be calculated by setting the overpotential $\Delta\phi_{R1C}$ for the 1C electric current under the ideal situation, i.e., $\mu_{(12)} = 0$, ϕ_0 is the reference electrical potential, and δ_{ij} is the Kronecker delta. Initially, the particle is assumed to be stress free, strain free and static, hence the initial values of the following variables are zero: $\boldsymbol{\sigma}$, $\boldsymbol{\varepsilon}^{(e)}$, $\boldsymbol{v}$, $\boldsymbol{v}^L_{(2)}$, and $\mu_{EX(12)}$.

To display the deformation of the particle directly, we need to calculate Z^i, which gives the coordinates of Sn in the lab space. The solved $v^L_{(2)i}$ should be transformed into the component in the lab space with the below equations. The derivation steps are shown in Appendix A8. The boundary condition for solving Z^i is $v^L_{(2)L1}(z^1 = 0) = 0$.

$$Z^1 = \sqrt{g_{(2)22}} \tag{2.3.30}$$

$$\frac{\partial Z^3}{\partial z^1} = -\sqrt{g_{(2)11} - \left(\frac{\partial Z^1}{\partial z^1}\right)^2} \tag{2.3.31}$$

$$\frac{\partial Z^3}{\partial z^3} = \sqrt{g_{(2)33} - \left(\frac{\partial Z^1}{\partial z^3}\right)^2} \tag{2.3.32}$$

$$v^L_{(2)i} = v^L_{(2)Lj}\frac{\partial Z^j}{\partial z^i} \tag{2.3.33}$$

$$\frac{\partial Z^i}{\partial t} = v^L_{(2)Li} \tag{2.3.34}$$

3. Results and discussions

In this paper, some material parameters of the Li-Sn system currently serve as placeholders for future simulation versatility for different lithium-ion battery binary systems. For example, the reference thermodynamic diffusion coefficient L_0, viscosities $\eta_H^{(e)}$, $\eta_D^{(e)}$, and $\eta_D^{(p)}$, symmetry factors $a^{(p)}$ and $a^{(R)}$, etc. Compared to the numerical error, the chosen material parameters may dominate the overall error in final results. Hence, analyzing the numerical error in the current simulations lacks practical significance and is neglected in the present theoretical study.

We simulate anode particles at three different C-rates: C-rate = 3, C-rate = 1.5 and C-rate = 0.75. The particles with all three C-rates are lithiated until their states of charge (SOC) are equal to 0.5. Once the SOCs reach 0.5, the particles start to relax, and the electric current decrease to zero within 5 s. The initial times of the relaxation ($t_R = 0$) are set when the SOCs reach 0.5. We have presented several key phenomena during the evolution in our simulations, namely molar fraction of occupied sites of Li ($y'_{(1)}$), velocity of Li continuum relative to Sn space ($\boldsymbol{v}_{(1)}$), mass center velocity relative to lab space ($\boldsymbol{v}^L = \boldsymbol{v} + \boldsymbol{v}^L_{(2)}$), hydrostatic elastic strain ($\varepsilon_H^{(e)} = \varepsilon^{(e)m}_m/3$), relative chemical potential ($\mu_{(12)}$), plasticity rate ($\lambda^{(p)}$), hydrostatic elastic stress ($\sigma_H = \sigma^m_m/3$), hydrostatic viscous stress ($\tau_H^{(e)} = \tau^{(e)m}_m/3$), hydrostatic Cauchy stress ($p_H = p^m_m/3$), and the evolution of whole cell voltage change as induced by anode $\Delta\phi = \phi_0 - \phi$. Please note that all the components are for the lab space and the values in the results are nondimensionalized if no unit is specified.

During lithiation, $y'_{(1)}$ and $\mu_{(12)}$ increase with a nonuniform distribution as displayed in Fig. 2. The higher $\mu_{(12)}$ near the arc makes Li move from the arc into the particle. The velocity of Li relative to the Sn space keeps decreasing during lithiation (Fig. 2) since the fraction of Li is increased. Equation (2.1.4) yields $\boldsymbol{J}_{(1)} = \rho_{(2)}x_{(1)}\boldsymbol{v}_{(1)}$, where $x_{(1)}$ increases from zero. Although $\rho_{(2)}$ decreases due to the volume expansion, $\boldsymbol{v}_{(1)}$ decreases from infinity with the constant lithiation rate. The distribution of $\boldsymbol{v}^L$ in Fig. 2 shows that the particle moves relatively faster on the connection region between the bottom and the arc. While the arc moves outward,

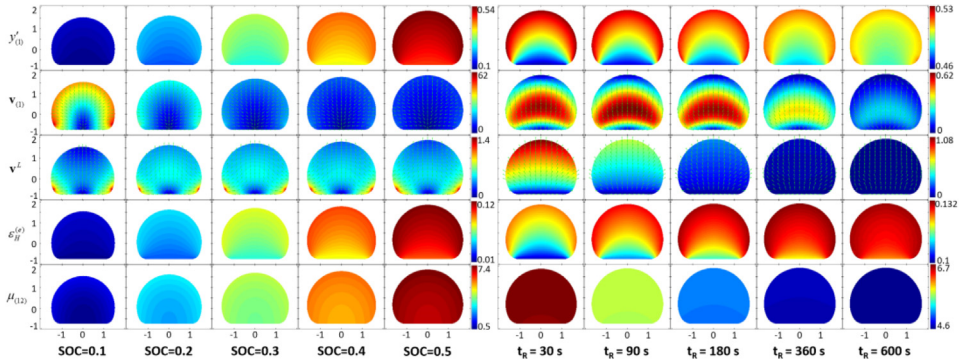

Fig. 2. A representative evolution of several key parameters in Sn particle: Molar fraction of occupied Li sites $y'_{(1)}$, velocity of Li continuum relative to the Sn space $\boldsymbol{v}_{(1)}$, mass center velocity relative to lab space $\boldsymbol{v}^L$, hydrostatic elastic strain $\varepsilon_H^{(e)}$, and relative chemical potential $\mu_{(12)}$ during lithiation (C-rate = 3) and relaxation. $y'_{(1)}$ and $\mu_{(12)}$ increase with uneven distributions during lithiation, which indicates the non-equilibrium state of the system. During relaxation, the distributions of all parameters are gradually even, which represents the gradually weakened non-equilibrum state. The particle volume continues to increase during whole process because $\varepsilon_H^{(e)}$ increases during both lithiation and relaxation.

the $\boldsymbol{v}^L$ on a portion of the arc points to the interior of the particle. This phenomenon indicates that the deformation of the particle boundary is combined of (1) the movement of the mass center continuum and (2) the generation of the mass center continuum by the chemical reaction on the surface.

In contrast to the increase and the nonuniform distribution of $\mu_{(12)}$ during lithiation, $\mu_{(12)}$ decreases with a tiny gradient during the relaxation, as displayed in Fig. 2. This observation indicates that the system approaches equilibrium. During relaxation, $\boldsymbol{v}_{(1)}$ in Fig. 2 shows that Li keeps diffusing towards the bottom. Hence, $y'_{(1)}$ increases near the bottom and decreases near the arc, as displayed in Fig. 2. The $\boldsymbol{v}_{(1)}$ on the arc is mostly tangential during relaxation, which makes $y'_{(1)}$ symmetric along the arc at the end of relaxation. The direction of $\boldsymbol{v}_{(1)}$ near the top of the particle points outward during relaxation. This result indicates that some Li may move out while the total electric current is zero. The particle volume keeps increasing during relaxation since $\varepsilon_H^{(e)}$ is increased.

With the increase of particle volume, $\lambda^{(p)}$ concentrates around the bottom as displayed in Fig. 3a. This trend indicates that the failure of the particle may initiate near the bottom because of the stronger plastic deformation occurring there. The particle lithiated at a higher C-rate shows a higher plasticity rate, suggesting a higher probability of failure. Fig. 3b shows that the maximum $\lambda^{(p)}$ in the particles of all three C-rates reach stable values during lithiation and decrease during relaxation, which means that the corresponding generalized driving force ψ are constrained to stable values by plastic deformation. This phenomenon is consistent with the yield stress in the ideal plasticity model.

The spontaneous increase of particle volume indicates the lower free energy at a larger volume. Then equation (2.1.30) yields $\sigma_H < 0$, which is demonstrated by Fig. 4 for all three C-rates. During the lithiation, the σ_H with a higher C-rate is more negative than that with a lower C-rate, which implies a faster decrease of free energy and a faster volume expansion. With increased SOC and C-rates, σ_H displays stronger nonuniform distribution. The most negative σ_H concentrates near the bottom of the particle. During relaxation, the distributions of σ_H in Fig. 4 appears more uniform with increases in t_R. σ_H approaches zero at the end of relaxation, which indicates the slowdown of free energy change.

Fig. 5 shows the evolution of $\tau_H^{(e)}$ during lithiation and relaxation. A higher C-rate leads to a higher strain rate, and hence a higher $\tau_H^{(e)}$. With an increased SOC, $\tau_H^{(e)}$ slightly decreases. This decrease may occur because the enlarged particle volume decreases the volume expansion rate. During relaxation, $\tau_H^{(e)}$ decreases because the strain rate decreases when the system approaches equilibrium.

The evolution of p_H is shown in Fig. 6. The particle is mostly in compression. p_H presents a more negative value when the C-rate is higher. The region around the bottom has stronger compression

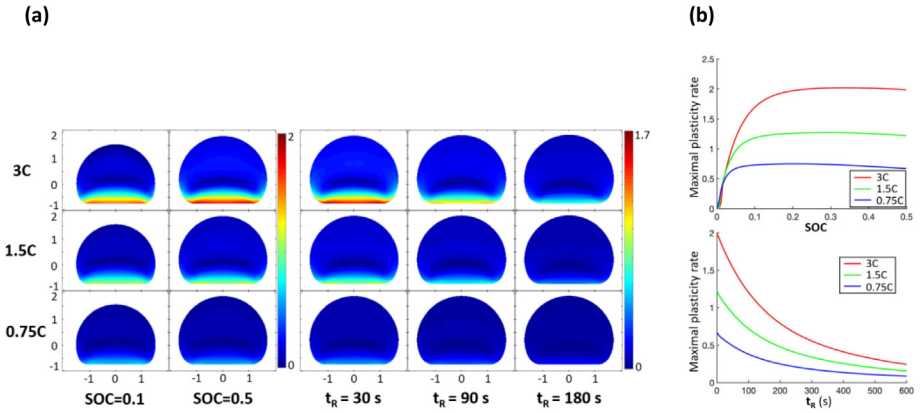

Fig. 3. (a) Plasticity rate $\lambda^{(p)}$ at SOC 0.1 and 0.5, followed by the relaxation until t_R = 180 s. The maximum plasticity rate locates near the bottom region of the particle. (b) Maximum plasticity rate in the particle during lithiation and relaxation with three different C-rates. During lithiation, the maximum $\lambda^{(p)}$ of every particle initially increases and till reaching to a constant value. A higher C-rate indicates a higher maximum $\lambda^{(p)}$.

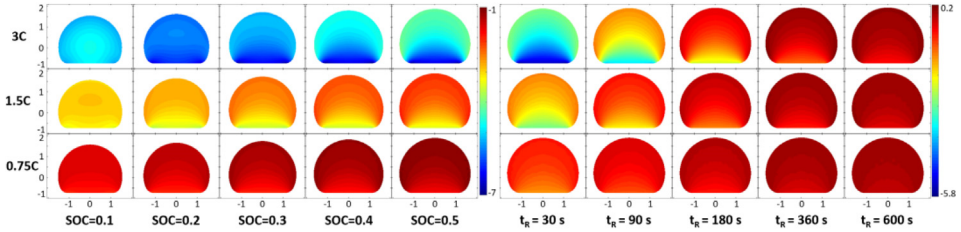

Fig. 4. Hydrostatic elastic stress σ_H during lithiation (SOC = 0.1–0.5) and relaxation (t_R = 30–600 s) at three different C-rates (3C, 1.5C, and 0.75C). σ_H becomes negative during lithaition at all C-rates. $\sigma_H < 0$ means that free energy is decreased when particle volume is increased. Volume expansion is hence a spontaneous behavior of the particle. A higher C-rate corresponds, σ_H becomes more negative, which implies a faster decrease of free energy and a faster volume expansion of the particle. During relaxation, σ_H with all C-rates get close to zero with gradually even distributions, which indicate the slowdown of free energy change.

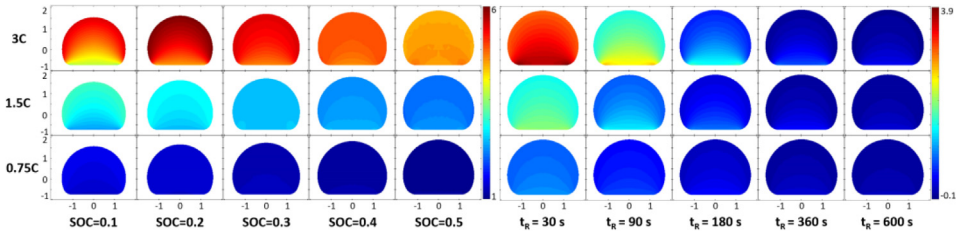

Fig. 5. Hydrostatic viscous stress $\tau_H^{(e)}$ during lithiation (SOC = 0.1–0.5) and relaxation (t_R = 30–600 s) at three different C-rates (3C, 1.5C, and 0.75C). A higher C-rate indicates a higher $\tau_H^{(e)}$ which slightly decreases with increased SOC. During relaxation, $\tau_H^{(e)}$ with all C-rates are close to zero with gradually even distributions, which indicate that particles approach to the equilibrium state.

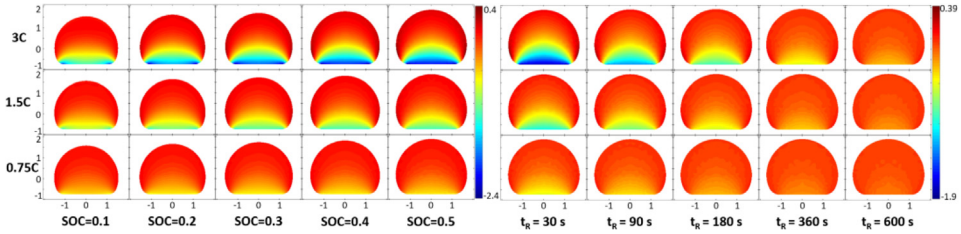

Fig. 6. Hydrostatic Cauchy stress p_H during lithiation (SOC = 0.1–0.5) and relaxation (t_R = 30–600 s) at three different C-rates (3C, 1.5C, and 0.75C). The negative value of p_H indicates that the particle is mostly in compression. The bottom region shows stronger compression than the bulk region due to the bonding between the particle and current collector. A higher C-rate and a higher SOC indicate a stronger uneven-distribution of p_H. The uneven distribution gradually disappears during relaxation, which indicates the particles approach to the equilibrium state.

than the bulk of the particle, due to bonding with the current collector. The p_H with a higher C-rate shows more noticeable nonuniform distribution. During relaxation, the nonuniform distribution gradually disappears and p_H approaches zero, which suggests a gradually weakened non-equilibrium state.

Fig. 7 displays the voltage change for an entire cell as induced by the anode particle. Three anode particles are lithiated with 3C, 1.5C, and 0.75C. The time equals to zero at the beginning of lithiation. Anode particles with 3 different C-rates reach 0.5 SOC when t = 600 s, 1200 s, and 2400 s, respectively. During the lithiation, the $\Delta\phi$ with the higher C-rate increases faster than the $\Delta\phi$ with a lower C-rate since more electrical energy is dissipated. All the particles relax to t = 3000 s once their SOC reaches 0.5. During relaxation, for all three C-rates, $\Delta\phi$ at first decreases steeply, then approaches stable values after gentle decreases. The steep decreases correspond to the relaxation of the chemical reaction. The gentle decreases correspond to diffusional relaxation. The particle with the higher C-rate needs longer time to relax in the polarizations induced by both chemical reaction and diffusion, due to the stronger non-equilibrium effects of the higher C-rate. The particle with the lower C-rate has a relatively higher final $\Delta\phi$. This finding suggests that the battery charged by the lower C-rate may supply more electrical energy, even though it has the same charge capacity.

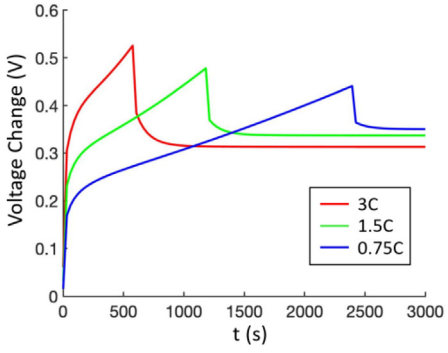

Fig. 7. The evolution of whole cell voltage change $\Delta\phi$ induced by the anode during charging/relaxation at three different C-rates. A higher C-rate indicates a higher $\Delta\phi$ during lithiation. The relaxation stage of $\Delta\phi$ for every C-rate includes a steep decrease followed by a gentle decrease. A higher C-rate corresponds to a lower final voltage change $\Delta\phi$. Thus the cell charged by a lower C-rate results in a higher voltage at the end of relaxation.

Although the bonding between the particle and the current collector restricts the deformation of the bottom region, the plasticity flow releases the elastic deformation of the particle. The maximum $\lambda^{(p)}$ locates around the bottom, as displayed in Fig. 3a. For 3C lithi-

ation, Fig. 3b shows that the $\lambda^{(p)}$ around the bottom has not reached the stable value yet when SOC = 0.1. This observation suggests that the plasticity deformation may not be enough to release the elastic deformation when SOC = 0.1. It is consistent with the distribution of $\tau_H^{(e)}$ in Fig. 5, by using equation (2.2.26). The particle with 3C lithiation has a noticeable nonuniform distribution of $\tau_H^{(e)}$ when SOC = 0.1. This occurs because the elastic strain rate around the bottom is restricted by bonding, while the $\lambda^{(p)}$ is not yet sufficient to release the volume expansion there. With the increased SOC during lithiation, $\lambda^{(p)}$ reaches the stable value as displayed in Fig. 3b, and the elastic strain rate is sufficiently released around the bottom. Hence, the distribution of $\tau_H^{(e)}$ in Fig. 5 appears more uniform during lithiation. During relaxation, the plasticity flow continues to release the elastic deformation and results in $\varepsilon_H^{(e)}$ and σ_H more uniformly distributed, as shown in Figs. 2 and 4. σ_H is related to $\varepsilon_H^{(e)}$ and $y'_{(1)}$. During relaxation, the uniformization of $\varepsilon_H^{(e)}$ and σ_H suggests the decrease of the gradient of $y'_{(1)}$, as shown in Fig. 2. When approaching to the equilibrium, $\lambda^{(p)}$ gets close to zero (Fig. 3b) since the driving force of $\lambda^{(p)}$ nearly vanishes, and σ_H is nearly zero and is uniformly distributed (Fig. 4).

The driving force of the plasticity flow depends on the elastic stress, as depicted in equation (2.2.18). To ensure $\lambda^{(p)}$ being higher around the bottom of the particle in lithiation/relaxation as displayed in Fig. 3a, ψ should be higher around the bottom. Maintaining this nonuniform distribution of ψ leads to the nonuniform distribution of σ_H between the bulk and the bottom, as shown in Fig. 4. σ_H and $\tau_H^{(e)}$ satisfy the equation $\sigma_H + \tau_H^{(e)} = p_H$ which is derived from equation (2.2.14). Since $\tau_H^{(e)}$ shows relatively uniform distribution in Fig. 5, the distribution of p_H in Fig. 6 looks similar to the distribution of σ_H in Fig. 4. Thus, the nonuniformly distributed p_H should be a necessary condition of the mechanical non-equilibrium process. During the lithiation, the distribution of both σ_H and p_H approach steady states as shown in Figs. 4 and 6 respectively. The steady states indicate the mechanical minimum entropy production in the particle, based on the principle of minimum entropy production in non-equilibrium thermodynamics (de Groot and Mazur, 2011). Minimizing the mechanical entropy production of the particle should be the essential reason why $\tau_H^{(e)}$ approaches a uniform distribution during lithiation in Fig. 5.

Compared with the higher C-rate, a lower C-rate leads to a slower volume expansion. The elastic strain rate with the lower C-rate is hence lower. This relation indicates that the necessary $\lambda^{(p)}$ for releasing the elastic deformation around the bottom is lower. This trend is consistent with the results in Fig. 3b. The particle requires a shorter process to reach the lower stable value of $\lambda^{(p)}$. This is the reason why the $\tau_H^{(e)}$ with the lower C-rate approaches the uniform distribution earlier than that with the higher C-rate, as displayed in Fig. 5. The lower $\lambda^{(p)}$ corresponds to the lower driving force ψ, which leads to a less nonuniform distribution of σ_H, as shown in Fig. 4. Hence, Fig. 6 shows that the p_H with the lower C-rate has a less nonuniform distribution.

The different C-rate corresponds to the different chemical reaction rate J_M, which depends on the $\Delta\phi$ and $\mu_{(12)}$ on the arc of the particle. For the 3C lithiation, Fig. 2 shows that $\mu_{(12)}$ keeps increasing on the arc. With the chemical reaction model in Section 2.2.2, Fig. 7 shows a consistent result that $\Delta\phi$ increases with the increased SOC during lithiation. During relaxation, the Li on the arc continues to diffuse into the interior of the particle, and the $\mu_{(12)}$ on the arc decreases due to the diffusion of Li, as displayed in Fig. 2. Based on the model of the chemical reaction, $\Delta\phi$ hence decreases with the $\mu_{(12)}$ during diffusional relaxation, as indicated in Fig. 7. This process is attributed to approaching an equilibrium state of the solution system. Fig. 7 suggests that particles for 3C, 1.5C and 0.75C are close to their equilibrium state at t = 1200 s/t_R = 600 s, t = 1550 s/t_R = 350 s and t = 2600 s/t_R = 200 s, respectively, where t_R is the relaxation time. We thus expect that other state functions, i.e., σ_H, $\tau_H^{(e)}$, and p_H, show similar distributions with respect to different C-rates near these time points. Fig. 4 shows that the distributions of σ_H on t_R = 600 s/3C are similar to the distribution of σ_H on t_R = 360 s/1.5C and t_R = 180 s/0.75C. Figs. 5 and 6 also show the same phenomenon for $\tau_H^{(e)}$ and p_H at the same time points. This consistency implies a coupling between the mechanics and electrochemistry of electrodes.

Some modeling studies (Bower et al., 2015; Cui et al., 2013, 2012) for the mechanical-diffusional coupling effects of electrodes specialized their formulations for the spherical particle with traction-free boundary condition, of which simulations were simplified to 1D. The equations in this study, by contrast, are suitable for generalized geometries. Di Leo et al. (2014) contributed the 2D finite element simulation for a spheroid electrode particle based on the finite deformation framework, but the plastic deformation was not included. Compared to the 1D simulations for traction-free spherical particles, the 2D simulation for the spherical cap particle bonded on current collector in this study illuminates the effect of plastic flow in a more realistic scenario: plastic flow can release the stress concentrated by the boundary constraint, as discussed above, and weaken the nonuniform distribution of Li in the particle, and finally help increase the effective capacity of the electrode. This effect agrees with the finite element simulation of a hollow double-walled Si nanotube anode by ; Di Leo et al. (2015): Li-ion concentration is uniformly distributed in the whole nanotube, and the plastic deformation induced by the tangential constraint concentrates at the interior surface of the nanotube (cf. Fig. 6 in Di Leo et al. (2015)). The effective capacity of the nanotube with plasticity is much higher than that without plasticity (cf. Fig. 9 in Di Leo et al. (2015)).

Because of the geometry differences, the Li-ion concentration in this study is noticeably nonuniform distributed than that in Di Leo et al. (2015). At the end of relaxation, the particle approaches its equilibrium state: $y'_{(1)}$ in Fig. 2 shows (1) a relatively higher value that evenly distributes along the arc section of the particle boundary, and (2) the sharp change at the connection between the arc and the bottom of the particle boundary (point C in Fig. 1a). These two phenomenon were also displayed in the cross section image of a Sn particle captured by the field emission scanning electron microscope (FESEM) in the study of Takeuchi (2016), in which the Sn particle was bonded on current collector and slowly lithiated (C-rate = 0.0146) by Li focused ion beams (Li-FIB). In addition, the FESEM image for the cross section of the Sn particle (cf. Fig. 1d in Takeuchi (2016)) shows a band of contrast in the bulk region near the implantation area of Li-FIB, which is not revealed in our simulation (Fig. 2). This difference may be attributed to the different boundary conditions of Li flux on particle surface: The localized Li-FIB had been shown to generate complicated local plastic deformation on the implantation area (cf. Fig. 1c in Takeuchi (2016)), which leads to the local unforeseen distribution of Li concentration due to the mechanical-diffusional coupling effect.

The mechanical-diffusional-electromechanical coupling effect in this study is formulated based on the continuity of state functions, as shown in Section 2.1, which yields the spatial continuity of θ and $\nabla\theta$ during the non-equilibrium process. Hence $\lambda^{(p)}$ and $\nabla\lambda^{(p)}$ should be continuous over space. This requirement is satisfied by the kinetic plasticity model $\lambda^{(P)} = \lambda^{(P)}(\psi)$ in Section 2.2.2, which is a continuous function without involving a specific yielding strength. When ψ is relatively tiny, $\lambda^{(P)}$ represents the stress-

induced creep. The kinetic plasticity model shows the similar response of plastic strain to the ideal plasticity model (Hill, 1998) when K_ψ in equations (2.2.21) and (2.2.22) is large enough. The smooth transition between the elastic region and plastic region of electrodes has been formulated using the piecewise power functions in Bower et al. (2011), Bower et al. (2015), Cui et al. (2012), Cui et al. (2013), and Di Leo et al. (2015). Compared to the piecewise plasticity models, the kinetic plasticity model helps simplify the procedure of solving the system equations by excluding the radial return algorithm (Simo and Taylor, 1986; Wang and Atluri, 1994) used for locating the plastic region in the system.

The chemical potential model that includes the finite deformation of electrodes has been studied by Cui et al. (2012), Cui et al. (2013), in which the mechanical part of the chemical potential model has a coefficient term $\left(\frac{\partial \boldsymbol{F}^e}{\partial c}\right)_{\boldsymbol{F},\boldsymbol{C}}$ that represents the deformation change induced by the concentration change for the intermediate state under the fixed total deformation and the fixed stiffness. However, $\left(\frac{\partial \boldsymbol{F}^e}{\partial c}\right)_{\boldsymbol{F},\boldsymbol{C}}$ relates to not only the material property (i.e., the expansion ratio) but also the change of elastic state, which is implicit and needs to be solved. In contrast, the relative chemical potential model in this study uses the material property K_D only to explicitly show the mechanical part. In some other studies of modeling the finite deformation of electrodes, e.g., Bower et al. (2011), Dal and Miehe (2015), Di Leo et al. (2014), Di Leo et al. (2015), and Bucci et al. (2016), the chemical potential are modeled based on the Larche-Cahn model (Larché and Cahn, 1973) shown in equation (1.1). However, the Larche-Cahn model (Larché and Cahn, 1973) is based on the assumptions that (1) the deformation of the system is small and thermodynamically reversible and (2) the molar mass of Li-ion is much less than the molar mass of site component, $M_{(1)} \ll M_{(2)}$. The assumption of small deformation would result in the metric change negligible. Thermodynamic reversibility would result in the integral to be path independent. $M_{(1)} \ll M_{(2)}$ indicates constant density and $\boldsymbol{v} = \boldsymbol{0}$, which linearize the rate equations (2.2.12), (2.2.45), and (2.2.46). Then directly integrating the rate equations yields the Larche-Cahn model, which is a special case of the non-equilibrium model in this study. Using the Larche-Cahn model suggests the acceptance of above two assumptions. However, the assumption (1) is limited in the infinitesimal deformation and an equilibrium process. The assumption (2) oversimplifies the diffusion of Li since the molar mass of Li should not be negligible for most electrode materials. Therefore, it is not plausible to adopt the Larche-Cahn model to describe the chemical potential of electrodes with finite deformation or non-equilibrium process.

As Li atoms should share the stress of electrodes, we consider the movement of lithium as a part of the deformation of the mixtured system represented by the mass center contiuum. The deformation of the mixtured system should be formulated based on the mass-conserved infinitesimal element instead of the mole-number-conserved infinitesimal element, because the different molar mass of components make the mass conservation conflicted with the mole-number-conservation in the infinitesimal element of mass center continuum. Thus, we use the mass fractions of components instead of the concentration of components, and the specific free energy instead of the free energy density to formulate the mixtured system. In the existing studies for modeling the finite deformation of electrodes (Bower et al., 2011; Di Leo et al., 2014, 2015; Dal and Miehe, 2015; Bucci et al., 2016; Cui et al., 2013, 2012), by contrast, the concentration of components and the free energy density are used in the formulations based on the mole-number-conservation, suggesting that the movement of Li atoms are not considered as a part of the deformation of the mixture.

The mass-conserved infinitesimal element of the mixtured system is introduced by using multi metric spaces, in which every space reveals the deformation of every corresponding component in the mixture. The method of multi metric spaces helps distribute the strains of the mixtured system conveniently: the Li-Sn system includes three metric spaces (i.e., mass center space, Sn space, and lab space), in which the Sn space is selected as the reference space because (1) the elastic strain and the plastic strain rate of the mixture are assigned to the Sn continuum due to the interstitial mixing of the Li-Sn system, and (2) the Sn space is the Lagrangian space of the Sn continuum, which satisfies the requirement of the additive decomposition of strain component (equation (2.1.11)) derived from the metric-based definition of the finite strain (equation (2.1.10)). Compared to the multiplicative decomposition of deformation gradient used in the other modeling works for finite deformation of electrodes (Bower et al., 2011; Di Leo et al., 2014, 2015; Bucci et al., 2016; Cui et al., 2013, 2012), the additive decomposition of strain component is linear, simpler and also valid for the finite deformation of electrodes.

The method of multi metric spaces in this study reveals the diffusion-induced creep of electrodes. In the Li-Sn system described in the Sn space (i.e., reference space), the influences of diffusion-induced creep on the mixture (i.e., mass center continuum) are represented by the diffusion-induced convective effects, which are indicated by the terms including $\boldsymbol{v}$ (i.e., the mass center velocity relative to the reference space) in rate equations (2.2.12), (2.2.45) and (2.2.46). In the relation between the electrical potential and Li concentration of a Si film electrode measured by Pharr et al. (2014), the electrical potential showed transient trend reversal with each change of C-rate during lithiation, and the rate of the trend reversal is higher when the change of C-rate is larger (cf. Fig. 1 in Pharr et al. (2014)). This phenonmenon may be explained by the influcence of diffusion-induced creep: At the moment of instantly increasing the C-rate of the Si film electrode during lithiation, in the region of chemical reaction, $\varepsilon^{(e)}_{kj}\frac{\partial v^k}{\partial z^l}$ and $v^k\frac{\partial \varepsilon^{(e)}_{ij}}{\partial z^k}$ in equation (2.2.12) increase instantly, while the change of $\frac{\partial \varepsilon^{(e)}_{ij}}{\partial t}$ may keep negligible because of the viscosity of the electrode. Then increased $\dot{e}^{(e)}_{ij}$ may decrease $d\mu_{(12)}/dt$ by equations (2.2.46) and (2.2.47) since $K_D < 0$. Finally, the slope $\partial\phi/\partial t$ is increased by equation (2.2.32). ϕ hence transiently increases after each instant decrease induced by increasing the C-rate, and vice versa. When the change of C-rate is larger, the changes of terms $\varepsilon^{(e)}_{kj}\frac{\partial v^k}{\partial z^i}$ and $v^k\frac{\partial \varepsilon^{(e)}_{ij}}{\partial z^k}$ in equation (2.2.12) are larger, finally the trend reversal of ϕ is faster. As ϕ is influenced by $\boldsymbol{v}$ in equation (2.2.12), the diffusion-induced creep should take part in the mechanical-diffusional-electrochemical coupling effect of electrodes.

As the influence of the diffusion-induced creep, the terms including $\boldsymbol{v}$ in rate equations (2.2.12), (2.2.45) and (2.2.46) make the integrals for elastic strain, elastic stress, and relative chemical potential related to the history of diffusion. Furthermore, the elastic stress is influenced by the rate of deformation, because of the viscous stress $\boldsymbol{\tau}^{(e)}$ in equations (2.2.14) and (2.2.23). Therefore, the states of a mixtured system relate to the history and the rate of the evolution of the system, which is an essential feature of the non-equilibrium process. Compared to the framework that is based on the rate functions for modeling the non-equilibrium process of electrodes in this study, the formulations in existing contributions (Bower et al., 2011; Di Leo et al., 2014, 2015; Bucci et al., 2016; Cui et al., 2013, 2012) are based on the assumed explicit expressions of the free energy density without considering the viscosity and diffusion-induced creep, which are only suitable for the systems in quasi-equilibrium process.

4. Conclusion

In this paper, we have developed a general theory to describe the evolution of a solid solution system with finite deformation. The system is considered as a non-equilibrium process rather than a quasi-equilibrium process. This fully self-consistent theory is hence formulated based on rate functions. Mechanics, diffusion, phase separation, chemical reaction and electrical potential of the system are coupled with each other in the formulation. The key function of the coupling is the rate of the relative chemical potential that depends on the elastic strain rate and Li-ion fraction rate. The general theory has been applied to a simplified Li-Sn system in Li-ion batteries. We set multiple metric spaces to clarify the influence of the diffusion-induced creep of the system and to help assign different strains conveniently. During the non-equilibrium process of the Li-Sn system, the entropy production rate of the system is composed of a mechanical component, a diffusional component, and a chemical reaction component. The mechanical part is comprised of viscosity and plasticity and where the linearized viscosity is used. The plasticity and chemical reaction are formulated based on the transition-state theory. The kinetic formulation of the plasticity generates a continuous interface between elastic deformation and plastic deformation which helps obviate the steps of identifying the plastic region in the system and simplify the procedure of solving the plasticity of electrodes.

Three Sn electrode particles with initial spherical cap geometries and appropriate boundary conditions have been numerically simulated using the finite difference method coded with MATLAB. We have compared the lithiated processes of the particles with three different C-rates, including the lithiation and relaxation. The simulation results show that the bottom region of each particle has more plastic deformation than the bulk region. The plastic deformation helps release the volume expansion around the bottom region, although it is bonded. The particle with a higher C-rate needs a longer process to obtain higher rate of plastic deformation, which releases the faster volume expansion around the bottom. During lithiation, the electrical potential of the particle with a higher C-rate shows more polarization. After relaxation, the particle with a lower C-rate consists more electric energy, even though the final electric capacities of all particles are the same.

With the rigorous mathematical formulation, we illuminate the evolution of a solid solution system in details. Our developed theory and simulation help better understand the mechanical-diffu sional-electrochemical coupling effect in Li-ion batteries. Some innovations in this study, such as multiple metric spaces for different components, diffusion-induced creep/convection, viscosity, and kinetic plasticity, may provide more insight into the description of continuous mixtures especially at non-equilibrium.

Declaration of Competing Interest

The authors declare that they have no known competing financial interests or personal relationships that could have appeared to influence the work reported in this paper.

Appendix A

A1. Introduction to the metric-based kinematics of finite deformation

The initial configuration and the deformed configuration of a continuum correspond to two spaces with curvilinear coordinate frames $(\zeta^1,\zeta^2,\zeta^3)$ and (η^1,η^2,η^3) respectively. The differential of radius vector is invariant in both spaces: $d\boldsymbol{r}=\frac{\partial \boldsymbol{r}}{\partial \zeta^i}d\zeta^i=\frac{\partial \boldsymbol{r}}{\partial \eta^j}d\eta^j$. The basis of initial space and deformed space are defined by $\boldsymbol{e}_i=\frac{\partial \boldsymbol{r}}{\partial \zeta^i}$ and $\hat{\boldsymbol{e}}_j=\frac{\partial \boldsymbol{r}}{\partial \eta^j}$ respectively, where ^ denotes the deformed space. With the function relation $\zeta^i=\zeta^i(\eta^1,\eta^2,\eta^3)$, we have $d\boldsymbol{r}=d\eta^j\hat{\boldsymbol{e}}_j=d\zeta^i\boldsymbol{e}_i=\frac{\partial \zeta^i}{\partial \eta^j}d\eta^j\boldsymbol{e}_i$, which yields

$$\hat{\boldsymbol{e}}_j=\frac{\partial \zeta^i}{\partial \eta^j}\boldsymbol{e}_i \tag{A1.1}$$

The function relation $\eta^i=\eta^i(\zeta^1,\zeta^2,\zeta^3)$ yields

$$d\eta^i=\frac{\partial \eta^i}{\partial \zeta^j}d\zeta^j \tag{A1.2}$$

Equations (A1.1) and (A1.2) show the transformations between two spaces for the basis and components of $d\boldsymbol{r}$ respectively. Quantities which transform like the basis of $d\boldsymbol{r}$, by equation (A1.1), is named *covariant*. Quantities which transform like the components of $d\boldsymbol{r}$, by equation (A1.2), is named *contravariant*. Please note the different locations of the dummy indices in equation (A1.1) and equation (A1.2). The transformations for covariant quantities and contravariant quantities are mutually inverse. The indices of covariant quantities are subscripts. The indices of contravariant quantities are superscripts. A pair of the same indices that one is subscript and the other is superscripts indicates the Einstein summation convention.

The *metric* of a space is defined as the dot product between two base vectors of the space. The metric of the initial space is $g_{ij}=\boldsymbol{e}_i\cdot\boldsymbol{e}_j$. The contravariant metric g^{ij} is the inverse of g_{ij}: $[g^{ij}]=[g_{ij}]^{-1}$. We use g^{ij} to introduce the contravariant basis of the initial space: $\boldsymbol{e}^j=g^{ij}\boldsymbol{e}_i$. The deformed space also has the corresponding metric $\hat{g}_{ij}$ and contravariant basis $\hat{\boldsymbol{e}}^i$.

Based on the invariance of tensors, a 1st order tensor $\boldsymbol{A}$ and a 2nd order tensor $\boldsymbol{T}$ respectively satisfy below equations:

$$\boldsymbol{A}=A^i\boldsymbol{e}_i=A_i\boldsymbol{e}^i=\hat{A}^i\hat{\boldsymbol{e}}_i=\hat{A}_i\hat{\boldsymbol{e}}^i \tag{A1.3}$$

$$\boldsymbol{T}=T^{ij}\boldsymbol{e}_i\boldsymbol{e}_j=T_{ij}\boldsymbol{e}^i\boldsymbol{e}^j=T^i_j\boldsymbol{e}_i\boldsymbol{e}^j=\hat{T}^{ij}\hat{\boldsymbol{e}}_i\hat{\boldsymbol{e}}_j=\hat{T}_{ij}\hat{\boldsymbol{e}}^i\hat{\boldsymbol{e}}^j=\hat{T}^i_j\hat{\boldsymbol{e}}_i\hat{\boldsymbol{e}}^j \tag{A1.4}$$

where T^i_j and $\hat{T}^i_j$ are called mixed components of $\boldsymbol{T}$. The contravariant components, covariant components, and mixed components of $\boldsymbol{T}$ in different spaces are transformed by $\hat{T}^{ij}=T^{kl}\frac{\partial \eta^i}{\partial \zeta^k}\frac{\partial \eta^j}{\partial \zeta^l}$, $\hat{T}_{ij}=T_{kl}\frac{\partial \zeta^k}{\partial \eta^i}\frac{\partial \zeta^l}{\partial \eta^j}$, and $\hat{T}^i_j=T^k_l\frac{\partial \eta^i}{\partial \zeta^k}\frac{\partial \zeta^l}{\partial \eta^j}$ respectively.

The metric of a space can be used to change the indices location of the tensor components in the space. For example, $A^i=A_jg^{ij}$, and $\hat{T}_{ij}=\hat{T}^{kl}\hat{g}_{ki}\hat{g}_{lj}=\hat{T}^l_i\hat{g}_{lj}$. It can be proved that g_{ij} and g^{ij} are respectively the covariant and contravariant components of a tensor $\boldsymbol{g}$, named the *fundamental metric tensor*, whose mixed components are equal to the Kronecker delta: $g^i_k=\boldsymbol{e}^i\cdot\boldsymbol{e}_k=g^{ij}g_{jk}=\delta^i_k$. The mixed components of $\boldsymbol{g}$ are usually used to change the indices of quantities. For example, the trace of $\boldsymbol{T}$ is calculated by

$$Tr(\boldsymbol{T})=\left(T^{ij}\boldsymbol{e}_i\boldsymbol{e}_j\right):\left(g_{kl}\boldsymbol{e}^k\boldsymbol{e}^l\right)=T^{ij}g_{kl}(\boldsymbol{e}_i\cdot\boldsymbol{e}^k)(\boldsymbol{e}_j\cdot\boldsymbol{e}^l)=T^{ij}g_{kl}g^k_ig^l_j$$
$$=T^{ij}g_{ij}=T^i_i=\hat{T}^i_i$$

We consider the configuration of a deformed continuum as a deformed space. The covariant component of strain for the space deformation is defined as half of the metric change of the space from initial state to final state, as shown below,

$$\varepsilon_{ij}=\frac{1}{2}\left(\tilde{g}_{ij}-\bar{g}_{ij}\right) \tag{A1.5}$$

where ε_{ij} is the covariant component of strain, $\tilde{g}_{ij}$ and $\bar{g}_{ij}$ are the metric of the final space and the initial space respectively. ε_{ij} can

be used to introduce two strain tensors with the same covariant components but different contravariant basis: $\overset{\sim}{\boldsymbol{\varepsilon}} = \varepsilon_{ij}\overset{\sim}{\boldsymbol{e}}^{i}\overset{\sim}{\boldsymbol{e}}^{j}$ and $\bar{\boldsymbol{\varepsilon}} = \varepsilon_{ij}\bar{\boldsymbol{e}}^{i}\bar{\boldsymbol{e}}^{j}$. The tensor $\overset{\sim}{\boldsymbol{\varepsilon}}$ is equivalent to the Green strain tensor when the initial space is undeformed, which is proved below: The final metric and the initial metric are $\hat{g}_{ij}$ and g_{ij} respectively, which indicates $\hat{\varepsilon}_{ij} = \frac{1}{2}(\hat{g}_{ij} - g_{ij})$, where the ^ in $\hat{\varepsilon}_{ij}$ emphasizes the basis of deformed space for strain tensor. With $F^i_j = \frac{\partial \zeta^i}{\partial \eta^j}$, we have

$$\hat{\varepsilon}_{ij}\hat{\boldsymbol{e}}^i\hat{\boldsymbol{e}}^j = \frac{1}{2}\left(\hat{g}_{ij}\hat{\boldsymbol{e}}^i\hat{\boldsymbol{e}}^j - g_{ij}\hat{\boldsymbol{e}}^i\hat{\boldsymbol{e}}^j\right) = \frac{1}{2}\left(g_{kl}F^k_i F^l_j\hat{\boldsymbol{e}}^i\hat{\boldsymbol{e}}^j - g_{ij}\hat{\boldsymbol{e}}^i\hat{\boldsymbol{e}}^j\right) \tag{A1.6}$$

$$\begin{aligned}\hat{\varepsilon}_{ij}\hat{\boldsymbol{e}}^i\hat{\boldsymbol{e}}^j &= \frac{1}{2}\left[(\boldsymbol{e}_k\cdot\boldsymbol{e}_l)F^k_i F^l_j\hat{\boldsymbol{e}}^i\hat{\boldsymbol{e}}^j - g_{ij}\hat{\boldsymbol{e}}^i\hat{\boldsymbol{e}}^j\right]\\ &= \frac{1}{2}\left[\left(F^k_i\hat{\boldsymbol{e}}^i\boldsymbol{e}_k\right)\cdot\left(F^l_j\boldsymbol{e}_l\hat{\boldsymbol{e}}^j\right) - g_{ij}\hat{\boldsymbol{e}}^i\hat{\boldsymbol{e}}^j\right]\end{aligned} \tag{A1.7}$$

The deformation gradient is a two-point tensor, which includes the basis of two different spaces. As the initial space is undeformed, $g_{ij}\hat{\boldsymbol{e}}^i\hat{\boldsymbol{e}}^j = \boldsymbol{I}$. We hence have,

$$\hat{\boldsymbol{\varepsilon}} = \frac{1}{2}\left(\boldsymbol{F}^T\cdot\boldsymbol{F} - \boldsymbol{I}\right) \tag{A1.8}$$

where the right side is the definition of Green strain tensor.

When we decompose a deformation to multiple sequential processes, we have the multiplicative decomposition of deformation gradient and the additive decomposition of strain component. The additive decomposition of strain component (equation (2.1.11)) is proved as below: For simplicity, we consider two sequential processes for a deformation, (a) and (b). Based on equation (A1.5), the covariant component of strain for the process (a) is

$$\hat{\varepsilon}^{(a)}_{ij} = \frac{1}{2}\left(\tilde{g}{}^{(a)}_{ij} - \bar{g}^{(a)}_{ij}\right) = \frac{1}{2}\left(\tilde{g}{}^{(a)}_{ij} - g_{ij}\right) \tag{A1.9}$$

and the covariant component of strain for the process (b) is

$$\hat{\varepsilon}^{(b)}_{ij} = \frac{1}{2}\left(\tilde{g}{}^{(b)}_{ij} - \bar{g}^{(b)}_{ij}\right) = \frac{1}{2}\left(\hat{g}_{ij} - \bar{g}^{(b)}_{ij}\right) \tag{A1.10}$$

Because processes (a) and (b) are sequential, we have $\tilde{g}{}^{(a)}_{ij} = \bar{g}^{(b)}_{ij}$, summing equations (A1.9) and (A1.10) yields the additive decomposition below,

$$\hat{\varepsilon}_{ij} = \hat{\varepsilon}^{(a)}_{ij} + \hat{\varepsilon}^{(b)}_{ij} \tag{A1.11}$$

Hence, as two different mathematical forms of decomposing the finite deformation, the multiplicative decomposition of deformation gradient and the additive decomposition of strain component (equation (2.1.11)) are mutually consistent. Please note that only the covariant components in Lagrangian measure satisfy the additive decomposition of strain component.

In a curvilinear coordinate frame, the covariant derivative and Laplacian for scalars, and the covariant derivatives for the covariant/contravariant components of 1st and 2nd order tensors, are listed below:

$$\nabla_i\varphi = \frac{\partial\varphi}{\partial\zeta^i}$$

$$\nabla^2\varphi = \frac{\partial^2\varphi}{\partial\zeta^i\partial\zeta^j}g^{ij} - \frac{\partial\varphi}{\partial\zeta^k}\Gamma^k_{ij}g^{ij}$$

$$\nabla_i w^j = \frac{\partial w^j}{\partial\zeta^i} + w^k\Gamma^j_{ki}$$

$$\nabla_i w_j = \frac{\partial w_j}{\partial\zeta^i} - w_k\Gamma^k_{ji}$$

$$\nabla_i H^{jk} = \frac{\partial H^{jk}}{\partial\zeta^i} + H^{lk}\Gamma^j_{li} + H^{jl}\Gamma^k_{li}$$

$$\nabla_i H_{jk} = \frac{\partial H_{jk}}{\partial\zeta^i} - H_{mk}\Gamma^m_{ij} - H_{jm}\Gamma^m_{ik}$$

where Γ^k_{ij} is called Christoffel symbols. In Euclidean space and Riemannian Space, Christoffel symbols are calculated as below,

$$\Gamma^i_{jk} = \frac{1}{2}g^{is}\left(\frac{\partial g_{js}}{\partial\zeta^k} + \frac{\partial g_{ks}}{\partial\zeta^j} - \frac{\partial g_{jk}}{\partial\zeta^s}\right)$$

For more information about the metric-based continuum mechanics, see the reference Sedov (1997).

A2. Generalized mass conservation equation

A density function f of a continuum can be written as $f = f\left(Z^1, Z^2, Z^3, t\right)$ or $f = f(z^1, z^2, z^3, t)$. The rate of the volume integral of f depends on the local rate of f and the deformation of the domain of integration as shown below (Sedov, 1997):

$$\frac{d}{dt}\int_V f d\upsilon = \int_V\left[\left(\frac{\partial f}{\partial t}\right)_Z + \nabla\cdot\left(f\boldsymbol{v}^L_\upsilon\right)\right]d\upsilon \tag{A2.1}$$

where $\boldsymbol{v}^L_\upsilon$ is the velocity of the domain of integration of the continuum relative to the lab space. The rate of f for fixed Lagrangian coordinates of the continuum has two forms below:

$$\frac{df}{dt} = \left(\frac{\partial f}{\partial t}\right)_Z + \boldsymbol{v}^L_\upsilon\cdot\nabla f \tag{A2.2}$$

$$\frac{df}{dt} = \left(\frac{\partial f}{\partial t}\right)_z + \boldsymbol{v}_\upsilon\cdot\nabla f \tag{A2.3}$$

where $\boldsymbol{v}_\upsilon$ is the velocity of the domain of integration of the continuum relative to the reference space. The relation between $\boldsymbol{v}^L_\upsilon$ and $\boldsymbol{v}_\upsilon$ is

$$\boldsymbol{v}^L_\upsilon = \boldsymbol{v}_\upsilon + \underset{\sim}{\boldsymbol{v}} \tag{A2.4}$$

Substituting equations (A2.2), (A2.3), and (A2.4) into equation (A2.1) yields

$$\frac{d}{dt}\int_V f d\upsilon = \int_V\left[\left(\frac{\partial f}{\partial t}\right)_z + \nabla\cdot\left(f\boldsymbol{v}_\upsilon\right) + f\nabla\cdot\underset{\sim}{\boldsymbol{v}}\right]d\upsilon \tag{A2.5}$$

Based on mass conservation for component k, chemical reactions determine the variation of total mass which is equal to the variation of the volume integral of $\rho_{(k)}$, as shown in equations (A2.6) and (A2.7):

$$\frac{dm_{(k)}}{dt} = \int_V\sum_j\xi^{(j)}_{(k)}J^{(j)}d\upsilon \tag{A2.6}$$

$$\frac{dm_{(k)}}{dt} = \frac{d}{dt}\int_V\rho_{(k)}\left(z^1, z^2, z^3, t\right)d\upsilon \tag{A2.7}$$

Setting $f = \rho_{(k)}$ and $\boldsymbol{v}_\upsilon = \boldsymbol{v}_{(k)}$ in equation (A2.5) and combining equation (A2.6) yield equation (2.1.1).

A3. Entropy production rate

Combining equations (2.1.12), (2.1.14), (2.1.15) and the divergence theorem yields

$$\delta\int_V u\rho dV = \int_V\left[\rho\delta q + \sum_k\rho_{(k)}\left(\delta\boldsymbol{r}^L_{(k)} - \delta\boldsymbol{r}^L\right)\cdot\boldsymbol{F}^L_{(k)} + \boldsymbol{p}:\nabla\delta\boldsymbol{r}^L\right]dV \tag{A3.1}$$

Because $\rho dV = dm$, which is conserved mass differential, the variational of the total internal energy for the mass center continuum relates to the functional derivatives with respect to independent variables by

$$\delta\int_V u\rho dV = \int_V \left[\left(\frac{\delta U}{\delta s}\right)_{\boldsymbol{\varepsilon},x}\delta s + \sum_l \left(\frac{\delta U}{\delta \hat{\varepsilon}_{ij}^{(l)}}\right)_{s,\boldsymbol{\varepsilon}^{(l'\neq l)},x}\delta\hat{\varepsilon}_{ij}^{(l)} + \sum_k^{K-1}\left(\frac{\delta U}{\delta x_{(k)}}\right)_{s,\boldsymbol{\varepsilon},x_{(k'\neq k)}}\delta x_{(k)}\right]\rho dV \tag{A3.2}$$

Combining equations (A3.1) and (A3.2), setting $\delta s = ds$, $\delta\hat{\varepsilon}_{ij}^{(l)} = d\hat{\varepsilon}_{ij}^{(l)}$, $\delta x_{(k)} = dx_{(k)}$, $\delta q = dq$, $\delta \boldsymbol{r}_{(k)}^L = \boldsymbol{v}_{(k)}^L dt$, and $\delta \boldsymbol{r}^L = \boldsymbol{v}^L dt$ (variational are arbitrary and can be set following the real process), and using equation (2.1.4) yield

$$\rho T ds + \sum_l \hat{\sigma}^{(l)ij} d\hat{\varepsilon}_{ij}^{(l)} + \sum_k^{K-1}\rho\mu_{(kK)}dx_{(k)} = \rho dq + \sum_k^K \boldsymbol{J}_{(k)}\cdot\boldsymbol{F}_{(k)}^L dt + \boldsymbol{p}:\nabla\boldsymbol{v}^L dt \tag{A3.3}$$

We assume that $\boldsymbol{p}$ is a symmetric tensor. Using the kinematic relations equations (A3.4) and (A3.5) for strain rate and strains yields equation (A3.6):

$$\dot{e}_{ij} = \frac{1}{2}\left(\nabla_i v_j^L + \nabla_j v_i^L\right) \tag{A3.4}$$

$$\hat{\varepsilon}_{ij} = \sum_l \hat{\varepsilon}_{ij}^{(l)} \tag{A3.5}$$

$$\boldsymbol{p}:\nabla\boldsymbol{v}^L dt = \boldsymbol{p}:\dot{\boldsymbol{e}}dt = \hat{p}^{ij}d\hat{\varepsilon}_{ij} = \sum_l \hat{p}^{ij}d\hat{\varepsilon}_{ij}^{(l)} \tag{A3.6}$$

Then, substituting $\sum_k^K \boldsymbol{J}_{(k)} = 0$, the definition of heat flux $\rho dq = -\nabla\cdot\boldsymbol{J}_Q dt$, equations (2.1.26), (2.1.27), and (A3.6) into equation (A3.3) yields equations (A3.7), (A3.8), and (A3.9) for entropy change, entropy flow and entropy production rate, respectively. Using equations (A3.10) and (2.1.25) we have equation (2.1.24).

$$\rho\frac{ds}{dt} = -\nabla\cdot\boldsymbol{J}_S + \theta \tag{A3.7}$$

$$\boldsymbol{J}_S = \frac{1}{T}\left(\boldsymbol{J}_Q - \sum_k^{K-1}\mu_{(kK)}\boldsymbol{J}_{(k)}\right) \tag{A3.8}$$

$$T\theta = -\boldsymbol{J}_s\cdot\nabla T + \sum_l\left(p^{ij} - \sigma^{(l)ij}\right)\frac{\hat{d\varepsilon}_{ij}^{(l)}}{dt} - \sum_k^{K-1}\boldsymbol{J}_{(k)}\cdot\nabla\Psi_{(kK)}^L + \sum_j J^{(j)}A_C^{(j)} \tag{A3.9}$$

$$\hat{e}_{ij}^{(l)} = \frac{d\hat{\varepsilon}_{ij}^{(l)}}{dt} \tag{A3.10}$$

A4. Relative chemical potential

Because s is assumed to be independent of $\nabla x_{(1)}$ and $\nabla\boldsymbol{\varepsilon}^{(l)}$, we have

$$\left(\frac{\partial s}{\partial x_{(1)}}\right)_{T,\dots} = f\left(x_{(1)},\hat{\varepsilon}_{ij}^{(l)}\right) \tag{A4.1}$$

It yields

$$d\left[T\left(\frac{\partial s}{\partial x_{(1)}}\right)_{T,\dots}\right] = \left(\frac{\partial s}{\partial x_{(1)}}\right)_{T,\dots}dT + T\left(\frac{\partial^2 s}{\partial x_{(1)}^2}\right)_{T,\dots}dx_{(1)} + \sum_l T\left(\frac{\partial^2 s}{\partial x_{(1)}\partial\hat{\varepsilon}_{ij}^{(l)}}\right)_{T,\dots}d\hat{\varepsilon}_{ij}^{(l)} \tag{A4.2}$$

Based on the symmetry of the 2nd order derivatives of a_F, equations (2.1.30) and (2.1.31) yield

$$\sum_l T\left(\frac{\partial^2 s}{\partial x_{(1)}\partial\hat{\varepsilon}_{ij}^{(l)}}\right)_{T,\dots}d\hat{\varepsilon}_{ij}^{(l)} = \sum_l -\left(\frac{\partial\hat{\gamma}^{(l)ij}}{\partial x_{(1)}}\right)_{T,\dots}Td\hat{\varepsilon}_{ij}^{(l)} \tag{A4..3}$$

Substituting equation (A4.3) into equation (A4.2), we have

$$\left(\frac{\partial s}{\partial x_{(1)}}\right)_{T,\dots}dT + T\left(\frac{\partial^2 s}{\partial x_{(1)}^2}\right)_{T,\dots}dx_{(1)} = d\left[T\left(\frac{\partial s}{\partial x_{(1)}}\right)_{T,\dots}\right] + T\left(\frac{\partial\gamma}{\partial x_{(1)}}\right)_{T,\dots}\hat{g}^{ij}d\hat{\varepsilon}_{ij}^{(e)} \tag{A4.4}$$

Using equation (A4.4) in equation (2.1.33) yields

$$d\mu_{HOM(12)} = -d\left[T\left(\frac{\partial s}{\partial x_{(1)}}\right)_{T,\dots}\right] - T\left(\frac{\partial\gamma}{\partial x_{(1)}}\right)_{T,\dots}\hat{g}^{ij}d\hat{\varepsilon}_{ij}^{(e)} + \kappa\hat{g}^{ij}d\hat{\varepsilon}_{ij}^{(e)} + \left(\frac{\partial^2 u}{\partial x_{(1)}^2}\right)_{T,\dots}dx_{(1)} \tag{A4.5}$$

The parameter tensors with the 1st and 3rd orders are zero in isotropic material (Sedov, 1997). Using equation (2.1.29) we simplify equation (2.1.34) to

$$d\hat{\mu}_{INH(12)}^i = \hat{\omega}_{\nabla(12)}^{rspi}d\hat{\nabla}_p\hat{e}_{rs}^{(e)} + K_{(12)}\hat{g}^{iq}d\hat{\nabla}_q x_{(1)} \tag{A4.6}$$

with defining a material property

$$\frac{\partial^2 u}{\partial\hat{\nabla}_i x_{(1)}\partial\hat{\nabla}_q x_{(1)}} = \hat{K}_{\nabla(12)}^{iq} = K_{(12)}\hat{g}^{iq} \tag{A4..7}$$

The specific entropy s is related to the molar entropy s_M composed of a fraction part $s_{MF} = s_{MF}\left(y'_{(1)}\right)$ and a deformation part $s_{MD} = s_{MD}\left(\varepsilon_{ij}^{(l)}\right)$ as shown below:

$$s = \frac{S}{m} = \frac{N_{(2)}N_B}{m}s_M = x_{(2)}\frac{N_B}{M_{(2)}}\left(s_{MF} + s_{MD}\right) \tag{A4.8}$$

The fraction part obeys the entropy of the ideal solution as shown below (DeHoff, 2006):

$$s_{MF} = -R\left[y'_{(1)}\ln y'_{(1)} + \left(1-y'_{(1)}\right)\ln\left(1-y'_{(1)}\right)\right] \tag{A4.9}$$

Equation (A4.9) yields

$$\frac{\partial}{\partial x_{(1)}}\left(x_{(2)}\frac{N_B}{M_{(2)}}s_{MF}\right)_{T,\dots} = -R\left[\frac{1}{M_{(1)}}\ln\frac{y'_{(1)}}{y'_{(2)}} - \frac{N_B}{M_{(2)}}\ln y'_{(2)}\right] \tag{A4.10}$$

We define the excess relative chemical potential as below:

$$\mu_{EX(12)} = \mu_{HOM(12)} + T\frac{\partial}{\partial x_{(1)}}\left(x_{(2)}\frac{N_B}{M_{(2)}}s_{MF}\right)_{T,\dots} \tag{A4.11}$$

Substituting equations (A4.8) and (A4.11) into equation (A4.5) yields

$$d\mu_{EX(12)} = \frac{N_B}{M_{(2)}}Tds_{MD} - T\left(\frac{\partial\gamma}{\partial x_{(1)}}\right)_{T,\dots}\hat{g}^{ij}d\hat{\varepsilon}_{ij}^{(e)} + \kappa\hat{g}^{ij}d\hat{\varepsilon}_{ij}^{(e)} + \left(\frac{\partial^2 u}{\partial x_{(1)}^2}\right)_{T,\dots}dx_{(1)} \tag{A4.12}$$

where γ is related to the stiffness and thermal expansion ratio as shown below

$$\hat{\gamma}^{(e)ij} = \gamma \hat{g}^{ij} = -\frac{\partial}{\partial \hat{\varepsilon}^{(e)}_{kl}}\left(\frac{\hat{\sigma}^{ij}_{HOM}}{\rho}\right)_{x_{(1)},\hat{\varepsilon}^{(e)}_{mn\neq kl}}\left(\frac{\partial \hat{\varepsilon}^{(e)}_{kl}}{\partial T}\right)_{\frac{\sigma_{HOM}}{\rho}} = -\left(\lambda_\rho \hat{g}^{ij}\hat{g}^{kl} + G_\rho \hat{g}^{ik}\hat{g}^{jl} + G_\rho \hat{g}^{il}\hat{g}^{jk}\right)\alpha_T \hat{g}_{kl} \tag{A4.13}$$

Thus the coupling coefficient in the relative chemical potential of a isotropic material is

$$K_D = \kappa - T\left(\frac{\partial \gamma}{\partial x_{(1)}}\right)_{T,\ldots} - \frac{T}{x_{(2)}}\gamma \tag{A4.14}$$

With defining a material property $h = \left(\frac{\partial^2 u}{\partial x^2_{(1)}}\right)_{T,\ldots}$, substituting equation (A4.14) into equation (A4.12) yields equation (2.2.46).

We assume $\hat{\mu}^i_{INH(12)}$ is a 1st order homogeneous function of $\hat{\nabla}_p \hat{\varepsilon}^{(e)}_{rs}$ and $\hat{\nabla}_q x_{(1)}$. Equation (A4.6) yields

$$\hat{\mu}^i_{INH(12)} = \hat{\omega}^{rspi}_{\nabla}\hat{\nabla}_p \hat{\varepsilon}^{(e)}_{rs} + K_{(12)}\hat{g}^{iq}\hat{\nabla}_q x_{(1)} \tag{A4.15}$$

where $\hat{\omega}^{rspi}_{\nabla}$ for isotropic material satisfies

$$\hat{\omega}^{rspi}_{\nabla} = \omega_I \hat{g}^{rs}\hat{g}^{pi} + \omega_{IIA}\hat{g}^{rp}\hat{g}^{si} + \omega_{IIB}\hat{g}^{ri}\hat{g}^{sp} \tag{A4.16}$$

For simplicity, we assume $\omega_{IIA} = \omega_{IIB} = 0$. Combining equations (2.1.21), (A4.10), (A4.11), (A4.15) and (A4.16) yields equation (2.2.47). If $\left(\frac{\partial \gamma}{\partial x_{(1)}}\right)_{T,\ldots} = 0$, we have equation (2.2.48). Equation (2.2.49) is obtained from equation (A4.13).

A5. Transformed equations

We divide the relative chemical potential into a homogeneous-logarithm part and an inhomogeneous-excess part, $\mu_{(12)} = \mu_{HL(12)} + \mu_{IE(12)}$ with

$$\mu_{HL(12)} = RT\left[\frac{1}{M_{(1)}}\ln\frac{y'_{(1)}}{y'_{(2)}} - \frac{N_B}{M_{(2)}}\ln y'_{(2)}\right] \tag{A5.1}$$

Using equations (2.2.47) and (A5.1) yields equation (2.3.15). Combining equations (2.2.1), (2.2.2), (2.2.3), (2.2.28), (2.2.47), (2.3.2), (2.3.3), and (2.3.15) yields equations (2.3.1) and (2.3.6). Combining equations (2.1.12), (2.1.13), and $\boldsymbol{v}^L = \boldsymbol{v} + \boldsymbol{v}^L_{(2)}$ yields equation (2.3.4). Using equations (2.2.14) and (2.2.26) we have equation (2.3.5).

A6. Relation between D and L

Using equations (2.1.5) and (2.2.1), the flux of Li can be written as

$$\boldsymbol{J}_{(1)} = \rho_{(1)}x_{(2)}\boldsymbol{v}_{(1)} = c_{(1)}M_{(1)}x_{(2)}\boldsymbol{v}_{(1)} \tag{A6.1}$$

where $c_{(1)}$ is the concentration of Li. To estimate the relation between D and L, we only consider $\mu_{HL(12)}$ in the diffusion for simplicity, as shown below,

$$\boldsymbol{J}_{(1)} \approx -\frac{L}{T}\nabla\mu_{HL(12)} = -LR\left(\frac{1}{M_{(1)}y'_{(1)}y'_{(2)}} + \frac{N_B}{M_{(2)}y'_{(2)}}\right)\nabla y'_{(1)} \tag{A6.2}$$

The Fick's 1st law yields

$$c_{(1)}\boldsymbol{v}_{(1)} = -D\nabla c_{(1)} = -Dc_{MAX}\nabla y'_{(1)} = -D\frac{N_B\rho_{(2)}}{M_{(2)}}\nabla y'_{(1)} \tag{A6.3}$$

Combining equations (A6.1), (A6.2), (A6.3), and (2.2.29) yields the expression of D as shown below,

$$D = \frac{RL_0 f_L\left(M_{(2)} + M_{(1)}N_B y'_{(1)}\right)^2}{N_B\rho_{(2)}M^2_{(1)}M_{(2)}y'_{(1)}y'_{(2)}} \tag{A6.4}$$

A7. Differential of expanded surface area

Initially, the area differential of the particle surface is governed by

$$|dl_0|^2 = g^{\circ}_{(2)ij}dz^i dz^j = \left(dz^1\right)^2 + \left(dz^3\right)^2 \tag{A7.1}$$

and

$$|d\varsigma_0|^2 = g^{\circ}_{(2)22}\left(dz^2\right)^2 = \left(z^1\right)^2\left(dz^2\right)^2 \tag{A7.2}$$

where dl_0 is the initial length of the infinitesimal arc perpendicular to the initial basis vector $\boldsymbol{e}_2$ on the particle surface and $d\varsigma_0$ is the initial length of the infinitesimal arc parallel to the initial basis vector $\boldsymbol{e}_2$ on the particle surface. After the particle is deformed, the lengths of the infinitesimal arcs have

$$|dl|^2 = g_{(2)ij}dz^i dz^j = g_{(2)11}\left(dz^1\right)^2 + 2g_{(2)13}dz^1 dz^3 + g_{(2)33}\left(dz^3\right)^2 \tag{A7.3}$$

and

$$|d\varsigma|^2 = g_{(2)22}\left(dz^2\right)^2 = \left(Z^1\right)^2\left(dz^2\right)^2 \tag{A7.4}$$

where dl is the length of the infinitesimal arc perpendicular to the basis vector $\boldsymbol{e}_2$ on the particle surface and $d\varsigma$ is the length of the infinitesimal arc parallel to the basis vector $\boldsymbol{e}_2$ on the particle surface. Hence, the initial and present area differentials respectively have

$$(dA_0)^2 = |dl_0|^2|d\varsigma_0|^2 \tag{A7.5}$$

and

$$(dA)^2 = |dl|^2|d\varsigma|^2 \tag{A7.6}$$

Combining equations (A7.1), (A7.2), (A7.3), (A7.4), (A7.5), and (A7.6) yields equation (2.3.23).

A8. The component of $\boldsymbol{v}^L_{(2)}$ in the lab space

The relation between the components of a tensor in different coordinate frames yields equations (2.3.33) and (A8.1) (Sedov, 1997);

$$g_{(2)ij} = g^L_{pq}\frac{\partial Z^p}{\partial z^i}\frac{\partial Z^q}{\partial z^j} \tag{A8.1}$$

where g^L_{pq} is the metric of lab space. Using equation (A8.1) we have equation (2.3.30). If we assume $\frac{\partial Z^3}{\partial z^1} < 0$ and $\frac{\partial Z^3}{\partial z^3} > 0$, equation (A8.1) implies equations (2.3.31) and (2.3.32).

References

Vetter, J., Novák, P., Wagner, M.R., Veit, C., Möller, K.-C., Besenhard, J.O., Winter, M., Wohlfahrt-Mehrens, M., Vogler, C., Hammouche, A., 2005. Ageing mechanisms in lithium-ion batteries. J. Power Sources 147 (1-2), 269–281. https://doi.org/10.1016/j.jpowsour.2005.01.006.

Wang, D., Wu, X., Wang, Z., Chen, L., 2005. Cracking causing cyclic instability of LiFePO4 cathode material. J. Power Sources 140 (1), 125–128. https://doi.org/10.1016/j.jpowsour.2004.06.059.

Piper, D.M., Yersak, T.A., Lee, S.-H., 2013. Effect of compressive stress on electrochemical performance of silicon anodes. J. Electrochem. Soc. 160 (1), A77–A81. https://doi.org/10.1149/2.064301jes.

Shi, F., Song, Z., Ross, P.N., Somorjai, G.A., Ritchie, R.O., Komvopoulos, K., 2016. Failure mechanisms of single-crystal silicon electrodes in lithium-ion batteries. Nat. Commun. 7 (May), 1–8. https://doi.org/10.1038/ncomms11886.

Cheng, Y.-T., Verbrugge, M.W., 2009. Evolution of stress within a spherical insertion electrode particle under potentiostatic and galvanostatic operation. J. Power Sources 190 (2), 453–460. https://doi.org/10.1016/j.jpowsour.2009.01.021.
Kim, S., Huang, H.-Y., 2016. Mechanical stresses at the cathode–electrolyte interface in lithium-ion batteries. J. Mater. Res. 31 (22), 3506–3512. https://doi.org/10.1557/jmr.2016.373.
Kim, S., Wee, J., Peters, K., Huang, H.-Y., 2018. Multiphysics coupling in lithium-ion batteries with reconstructed porous microstructures. J. Phys. Chem. C 122 (10), 5280–5290. https://doi.org/10.1021/acs.jpcc.7b12388.
Kim, S., Chen, H., Huang, H.Y.S., 2019. Coupled mechanical and electrochemical analyses of three-dimensional reconstructed LiFePO4 by focused ion beam/scanning electron microscopy in lithium-ion batteries. J. Electrochem. Energy Convers. Storage 16 (1), 1–7. https://doi.org/10.1115/1.4040760.
Christensen, J., Newman, J., 2006. Stress generation and fracture in lithium insertion materials. J. Solid State Electrochem. 10 (5), 293–319. https://doi.org/10.1007/s10008-006-0095-1.
Bower, A.F., Guduru, P.R., Sethuraman, V.A., 2011. A finite strain model of stress, diffusion, plastic flow, and electrochemical reactions in a lithium-ion half-cell. J. Mech. Phys. Solids 59 (4), 804–828. https://doi.org/10.1016/j.jmps.2011.01.003.
Di Leo, C.V., Rejovitzky, E., Anand, L., 2014. A Cahn-Hilliard-type phase-field theory for species diffusion coupled with large elastic deformations: application to phase-separating Li-ion electrode materials. J. Mech. Phys. Solids 70 (1), 1–29. https://doi.org/10.1016/j.jmps.2014.05.001.
Bucci, G., Swamy, T., Bishop, S., Sheldon, B.W., Chiang, Y.-M., Carter, W.C., 2017. The effect of stress on battery-electrode capacity. J. Electrochem. Soc. 164 (4), A645–A654. https://doi.org/10.1149/2.0371704jes.
Larché, F., Cahn, J.W., 1973. A linear theory of thermochemical equilibrium of solids under stress. Acta Metall. 26 (1), 53–60. https://doi.org/10.1016/0001-6160(78)90201-8.
Huggins, R.A., 2008. Negative electrodes in lithium cells. Adv. Batter. 123–149. doi: 10.1007/978-0-387-76424-5_7.
Qi, Y., Hector Jr., L.G., James, C., Kim, K.J., 2014. Lithium concentration dependent elastic properties of battery electrode materials from first principles calculations. J. Electrochem. Soc. 161 (11), F3010–F3018. https://doi.org/10.1149/2.0031411jes.
Wen, J., Wei, Y., Cheng, Y.-T., 2018. Stress evolution in elastic-plastic electrodes during electrochemical processes: a numerical method and its applications. J. Mech. Phys. Solids 116, 403–415. https://doi.org/10.1016/j.jmps.2018.04.006.
Bower, A.F., Chason, E., Guduru, P.R., Sheldon, B.W., 2015. A continuum model of deformation, transport and irreversible changes in atomic structure in amorphous lithium–silicon electrodes. Acta Mater. 98, 229–241. https://doi.org/10.1016/j.actamat.2015.07.036.
Di Leo, C.V., Rejovitzky, E., Anand, L., 2015. Diffusion–deformation theory for amorphous silicon anodes: the role of plastic deformation on electrochemical performance. Int. J. Solids Struct. 67-68, 283–296. https://doi.org/10.1016/j.ijsolstr.2015.04.028.
Bower, A.F., Guduru, P.R., Chason, E., 2015. Analytical solutions for composition and stress in spherical elastic–plastic lithium-ion electrode particles containing a propagating phase boundary. Int. J. Solids Struct. 69-70, 328–342. https://doi.org/10.1016/j.ijsolstr.2015.05.018.
Dal, H., Miehe, C., 2015. Computational electro-chemo-mechanics of lithium-ion battery electrodes at finite strains. Comput. Mech. 55 (2), 303–325. https://doi.org/10.1007/s00466-014-1102-5.
Bucci, G., Chiang, Y.-M., Carter, W.C., 2016. Formulation of the coupled electrochemical–mechanical boundary-value problem, with applications to transport of multiple charged species. Acta Mater. 104, 33–51. https://doi.org/10.1016/j.actamat.2015.11.030.
Kang, B., Ceder, G., 2009. Battery materials for ultrafast charging and discharging. Nature 458 (7235), 190–193. https://doi.org/10.1038/nature07853.
Xie, J., Oudenhoven, J.F.M., Harks, P.-P., Li, D., Notten, P.H.L., 2015. Chemical vapor deposition of lithium phosphate thin-films for 3D all-solid-state li-ion batteries. J. Electrochem. Soc. 162 (3), A249–A254. https://doi.org/10.1149/2.0091503jes.
Thompson, A.P., Plimpton, S.J., Mattson, W., 2009. General formulation of pressure and stress tensor for arbitrary many-body interaction potentials under periodic boundary conditions. J. Chem. Phys. 131 (15), 154107. https://doi.org/10.1063/1.3245303.
Jones, R.B., 1965. Diffusion creep in polycrystalline magnesium. Nature 207 (70), 1965.
Pharr, M., Suo, Z., Vlassak, J.J., 2014. Variation of stress with charging rate due to strain-rate sensitivity of silicon electrodes of Li-ion batteries. J. Power Sources 270, 569–575. https://doi.org/10.1016/j.jpowsour.2014.07.153.
Whittingham, M.S., 2004. Lithium batteries and cathode materials. Chem. Rev. 104 (10), 4271–4302. https://doi.org/10.1021/cr020731c.
Song, Y.C., Li, Z.Z., Soh, A.K., Zhang, J.Q., 2015. Diffusion of lithium ions and diffusion-induced stresses in a phase separating electrode under galvanostatic and potentiostatic operations: phase field simulations. Mech. Mater. 91, 363–371. https://doi.org/10.1016/j.mechmat.2015.04.015.
ChiuHuang, C.-K., Shadow Huang, H.-Y., 2013. Stress evolution on the phase boundary in LiFePO 4 Particles. J. Electrochem. Soc. 160 (11), A2184–A2188. https://doi.org/10.1149/2.079311jes.
Cui, Z., Gao, F., Qu, J., 2013. Interface-reaction controlled diffusion in binary solids with applications to lithiation of silicon in lithium-ion batteries. J. Mech. Phys. Solids 61 (2), 293–310. https://doi.org/10.1016/j.jmps.2012.11.001.
Sedov, L.I., 1997. Mechanics of Continuous Media. World Scientific.
Sedov, L.I., 1965. Introduction to the Mechanics of a Continuous Medium. Addison-Wesley.
de Groot, S.R., Mazur, P., 2011. Non-equilibrium Thermodynamics. Dover Publications.
Gelfand, I.M., Fomin, S.V., 2000. The Calculus of Variations. Dover Publications.
Kearsley, E.A., Fong, J.T., 1975. Linearly independent sets of isotropic Cartesian tensors of ranks up to eight. J. Res. Natl. Bur. Stand. Sect. B Math. Sci. 79B (1), 49. https://doi.org/10.6028/jres.079b.005.
DeHoff, R., 2006. Thermodynamics in Materials Science. CRC Press, p. 624.
Persson, P.O., Strang, G., 2004. A simple mesh generator in MATLAB. SIAM Rev. 46 (2), 329–345. https://doi.org/10.1137/S0036144503429121.
Perrone, N., Kao, R., 1975. A general finite difference method for arbitrary meshes. Comput. Struct. 5 (1), 45–57. https://doi.org/10.1016/0045-7949(75)90018-8.
Takeuchi, S. et al., 2016. Editors' choice communication—comparison of nanoscale focused ion beam and electrochemical lithiation in β-Sn microspheres. J. Electrochem. Soc. 163 (6), A1010–A1012. https://doi.org/10.1149/2.1161606jes.
Zheng, Q., Mauro, J.C., 2017. Viscosity of glass-forming systems. J. Am. Ceram. Soc. 100 (1), 6–25. https://doi.org/10.1111/jace.14678.
Maxisch, T., Ceder, G., 2006. Elastic properties of olivine Lix FePO4 from first principles. Phys. Rev. B Condens. Matter Mater. Phys. 73 (17), 1–4. https://doi.org/10.1103/PhysRevB.73.174112.
Stournara, M.E., Guduru, P.R., Shenoy, V.B., 2012. Elastic behavior of crystalline Li-Sn phases with increasing Li concentration. J. Power Sources 208, 165–169. https://doi.org/10.1016/j.jpowsour.2012.02.022.
Shenoy, V.B., Johari, P., Qi, Y., 2010. Elastic softening of amorphous and crystalline Li-Si Phases with increasing Li concentration: a first-principles study. J. Power Sources 195 (19), 6825–6830. https://doi.org/10.1016/j.jpowsour.2010.04.044.
Ding, N. et al., 2009. Determination of the diffusion coefficient of lithium ions in nano-Si. Solid State Ionics 180 (2–3), 222–225. https://doi.org/10.1016/j.ssi.2008.12.015.
Shi, J., Wang, Z., Fu, Y.Q., 2016. Density functional theory study of diffusion of lithium in Li–Sn alloys. J. Mater. Sci. 51 (6), 3271–3276. https://doi.org/10.1007/s10853-015-9639-z.
Marcicki, J., Conlisk, A.T., Rizzoni, G., 2014. A lithium-ion battery model including electrical double layer effects. J. Power Sources 251, 157–169. https://doi.org/10.1016/j.jpowsour.2013.11.001.
Cui, Z., Gao, F., Qu, J., 2012. A finite deformation stress-dependent chemical potential and its applications to lithium ion batteries. J. Mech. Phys. Solids 60 (7), 1280–1295. https://doi.org/10.1016/j.jmps.2012.03.008.
Hill, R., 1998. The Mathematical Theory Of Plasticity. Oxford University Press, USA.
Simo, J.C., Taylor, R.L., 1986. A return mapping algorithm for plane stress elastoplasticity. Int. J. Numer. Methods Eng. 22 (3), 649–670. https://doi.org/10.1002/nme.1620220310.
Wang, L.H., Atluri, S.N., 1994. An analysis of an explicit algorithm and the radial return algorithm, and a proposed modification, in finite plasticity. Comput. Mech. 13 (5), 380–389. https://doi.org/10.1007/BF00512590.
Lide, D.R., 2005. CRC Handbook of Chemistry and Physics, Internet Version 2005, CRC Press. Taylor Fr. Boca Rat. FL, p. 2660. doi: 10.1016/0165-9936(91)85111-4.